The influence of olivine settling on the formation of basaltic cumulates revealed by micro-tomography and numerical simulations

Adrien J Mourey, Alexandre Carrara, Thomas Shea, Fidel Costa Rodriguez, Marc-Antoine Longpré

The influence of olivine settling on the formation of basaltic cumulates revealed by micro-tomography and numerical simulations

Adrien J. Mourey[1,2], Alexandre Carrara[3,4], Thomas Shea[1], Fidel Costa[2,5,6], Marc-Antoine Longpré[7]

[1]Department of Earth Sciences, University of Hawai'i at Mānoa, Honolulu, HI, USA

[2]Earth Observatory of Singapore, Nanyang Technological University, Singapore

[3]Department of Earth and Space Sciences, Box 35310, University of Washington, Seattle, WA, USA

[4]Université Clermont Auvergne, CNRS, IRD, OPGC, Laboratoire Magmas et Volcans, F-63000 Clermont-Ferrand, France

[5]Asian School of the Environment, Nanyang Technological University, Singapore

[6]Institut de Physique du Globe de Paris, Université Paris Cité, CNRS, France

[7]School of Earth and Environmental Sciences, Queens College, City University of New York, USA

Abstract

The speed at which crystals settle in magmatic reservoirs affects the solidification rate of magmas and their differentiation. Despite extensive prior work on the subject, most of our quantitative understanding of the process is still restricted to treating crystals as spherical particles and does not address the geometric complexities of natural crystals. Here, we use three-dimensional (3D) X-ray microcomputed tomography (X-μCT) observations on olivine crystals from Kīlauea Volcano (Hawai'i) to document their highly intricate and variable geometries, and the textural growth relationships between the olivine crystals and their inclusions (melt, spinel, and fluid/vapor bubbles). Olivine crystals generally have clustered polyhedral or skeletal shapes, which reflect variable magmatic conditions (or growth rates) during their formation. The cumulative presence of spinel, melt, fluid, and vapor inclusions affects the density of the host crystals by up to 6% relative, and thus plays a limited role on modifying crystal settling rate. In contrast, the overall crystal shape plays a major role. We performed numerical simulations employing a finite element method to investigate the effect of crystal morphology on settling rate and the evolution of the particle volume fraction in a magmatic convective layer. We show that for all olivine geometries investigated, the settling velocity is highest when the

long axis of the crystal is aligned with the flow direction of the melt. Increasing the aspect ratio of the olivine tends to decrease its settling velocity and results in an increase in the influence of its orientation on the terminal velocity (U_T). Extrapolation of the simulation results to variable particle volume fractions (Φ = 0-0.5) indicates high crystal settling rates (U_T = ~9.7 x 10^{-6} – 1.4 x 10^{-5} m/s) that are used to estimate the timescales for the formation of olivine cumulates in natural melt-dominated basaltic systems. The formation of olivine cumulates is therefore rapid, potentially leading to the accumulation of a crystal layer at the bottom, where the frictional contacts between the crystals exert a rheological lock-up acting against further convection. Crystal accumulation in the locked layer (parametrized with the solid/liquid volume ratio in the reservoir) is a function of the reservoir size and crystal fraction, and takes a few years in small reservoirs (less than 1 km thick) and a few decades in larger reservoirs (several kms thick). We propose a calibration of olivine suspension timescales for mafic magma reservoirs (based on the knowledge of the particle volume fraction, reservoir height, and olivine morphology). This calibration is used to estimate the rate of cumulate build-up, and can help interpret crystal size distributions in the framework of crystal suspension times.

Keywords

Olivine; crystal settling; crystal morphology; X-ray microcomputed tomography; numerical simulations

Highlights

- Solidification of a basaltic reservoir strongly depends on the settling rate of olivine
- Olivine terminal velocity is highest when the crystal long axis is aligned with the melt flow.
- Inclusions in olivine play a limited role on modifying crystal settling rate.
- Crystal accumulation in mafic systems takes a few years to a few decades.

1. Introduction

Crystal settling has been considered a ubiquitous process in magma reservoirs for a long time (Murata and Richter, 1966). Crystal settling is thought to control the mode of solidification of magmas on Earth (Martin and Nokes, 1988; Koyaguchi et al., 1990; Pankhurst et al., 2018a) and in planetary magma oceans (Elkins-Tanton, 2012). Quantifying the rate at which magma reservoirs solidify is essential for the understanding of their chemical differentiation through time. Differentiation of a cooling magma is a

mediated process by crystal nucleation and growth or dissolution, settling and reentrainment (by magma replenishment or assimilation). Crystal growth rates in basaltic magmas are relatively well quantified (e.g., Jambon et al., 1992; Arzilli et al., 2015; Mourey and Shea, 2019) and the reentrainment of negatively buoyant particles (entrainment of grains in convective layers) has been addressed experimentally (Solomatov et al., 1993a; Lavorel and Le Bars, 2009) and theoretically (Solomatov and Stevenson, 1993b). In most cases, the accumulation of crystal layers at the bottom of mafic reservoirs involves growth or reprecipitation of olivine crystals while in suspension in the melt, followed by mechanical settling, compaction through pressure, dissolution at grain contacts, and expulsion of the interstitial melt (e.g., Schmidt et al., 2012; Holness et al., 2017). Experimental studies have previously reproduced textures of olivine-rich layers (Schmidt et al., 2012), but the influence of crystal shape on settling remains poorly quantified.

The shape of natural olivine crystals is highly variable (e.g., equant, elongated, tabular, skeletal, hopper, dendrite) and is related to undercooling, cooling rate and the melt composition (e.g., Donaldson, 1976; Faure et al., 2003; Mourey and Shea, 2019). The well-faceted, polyhedral, tabular and hopper morphologies have been associated with relatively low undercooling ($-\Delta T < 25^{o}C$; Faure et al., 2003; Mourey and Shea 2019, where $-\Delta T$ is the temperature difference between the olivine liquidus and a temperature of interest below the liquidus), whereas skeletal and dendritic crystals are formed at moderate to high undercooling ($-\Delta T > 25^{o}C$; Faure et al., 2003; Mourey and Shea 2019). Polyhedral crystals were initially assumed to crystallize at near-equilibrium conditions (Pearce, 1984) and in a concentric “tree-ring” fashion (e.g., Clark et al., 1986). However, morphological remains of an early rapid growth (e.g., stepped hopper cavities) are commonly observed in polyhedral olivine phenocrysts (e.g., Welsch et al., 2013), challenging the assumption of near-equilibrium, low undercooling conditions. Instead, polyhedral olivine phenocrysts are considered to have an initial rapid growth history, forming a skeletal olivine framework that is progressively infilled as undercooling and growth rates decrease (e.g., Welsch et al., 2013; Mourey and Shea, 2019; Wallace et al., 2021).

Olivine is the most abundant mineral in Hawaiian eruptions, and the only mineral (along with Cr-spinel) within active summit reservoirs (e.g. Thornber et al., 2015). Moreover, both olivine and spinel are the

first minerals to crystallize in basaltic melts with >7 wt.% MgO (Roeder et al., 2001). Unsurprisingly, spinel inclusions are common in olivine crystals.

In this study, we demonstrate how modern X-ray microcomputed tomography (X-μCT) scans of olivine crystals can provide a wealth of new information on the three-dimensional (3D) distribution of melt inclusions, vapor bubbles, and spinels, in addition to the true 3D shape of crystals. The complexities of the inclusions network trapped in the crystals can help document crystal growth histories and thermal (undercooling) conditions.

We collected high-resolution X-μCT scans of three populations of olivine crystals from the 1820 Golden Pumice eruption (unit K1 from the Keanakāko'i Tephra) at Kīlauea Volcano (Hawai'i). We document the internal complexities (melt inclusion, vapor bubble and spinel fractions) of well-faceted polyhedral crystals and more skeletal crystals, and interpret those complexities in terms of crystal growth conditions. Using numerical simulations, we test how different olivine morphologies affect settling velocities, with implications for the timescales of olivine-rich mush and dunite cumulate formation. We quantify how the volume fraction of inclusions impacts a crystal's density and terminal velocity. To investigate the influence of crystal morphology on settling, realistic crystal morphologies identified with X-μCT scans are used to define initial crystal meshes with equal volumes and mass. The meshes are then integrated into numerical simulations of melt flow around the crystal employing the finite element method. The simulations explore the influence of the orientation of olivine crystals with the flow direction of the melt and the influence of their shape on the settling velocities. These velocities are then used to estimate settling timescales as a function of the crystal fraction and the reservoir size. Those timescales bring important new constraints on the rates at which cumulates and mush piles may form in mafic reservoirs, and can help petrologists better interpret crystal population characteristics (e.g. size distributions) in the light of suspension and accumulation rates.

2. Methods

2.1. Sample description

We used a sample from the Unit K1 (formerly Golden Pumice) eruption that occurred around 1820 C.E. during the explosive Keanakāko'i Tephra eruptive period at Kīlauea (Fig.1; Swanson et al., 2012). The eruption consisted in high lava fountains that produced fall deposits comprising chiefly rapidly cooled golden pumice with sparse lithic materials. The sample is glassy with 6.8 – 9.1 wt.% MgO in

120 the glass (Lynn et al., 2017) and contains different olivine populations (Fo_{80-89} (Fo = Mg/[Mg+Fe] in
121 mol.%; Lynn et al. 2017; Mourey et al., 2022). No other phenocryst phases were found.
122
123 **2.2 X-ray micro-tomography**
124 In volcanology, X-μCT has been used to measure the 3D shape and distribution of vesicles in volcanic
125 rocks (e.g., Polacci et al., 2006), quantify bubbles nucleation and growth in multiphase systems
126 (Oppenheimer et al., 2021), and characterize the morphology and chemical zoning of olivine crystals
127 (Pankhurst et al., 2014; 2018b; Mourey and Shea, 2019). Traditionally, the interpretation of mineral
128 textures is based on 2D images obtained with optical and electron microscopy. 2D images may lead to
129 inaccurate or erroneous interpretations when addressing the complexities of 3D morphologies (e.g.,
130 Mourey and Shea, 2019). The extrapolation to 3D from 2D images can be made by time-consuming
131 and destructive techniques involving serial sectioning and grinding method (e.g., Byron et al., 1995;
132 Daniel and Spear, 1999; Mock and Jerram, 2005). This method however results in low resolution in
133 the direction perpendicular to the observed plane, and most of the material is unfortunately destroyed
134 during polishing. Therefore, only partial records of the complexities of a 3D crystal are observed in 2D
135 sections. Recent advances in X-ray computed microtomography (X-μCT) during the last three
136 decades better allow accessing real 3D information. This technique affords proper interpretation of the
137 spatial relationships between textural and, sometimes, geochemical characteristics. X-μCT is non-
138 destructive and high spatial resolutions (sub-micron) can be attained.
139
140 The 1820 C.E. golden pumices were first gently crushed with a mortar and pestle, and a
141 representative variety of olivine morphologies were hand-picked for X-μCT scans. The crystals were
142 coated with glass and, to make crystal faces more apparent, they were immersed in a 1 normal HF
143 solution and cleaned (e.g., Lynn et al., 2017). Crystals were then mounted on carbon tape, carbon
144 coated, and imaged with a JEOL-8500 field emission gun electron microprobe at the University of
145 Hawai‘i. A selection of crystals (n=13) were scanned at the X-μCT facility at the University of Austin
146 Texas using an X-ray tube-based scanner (cone-beam geometry, Xradia MicroXCT-400). Each crystal
147 was individually mounted on the rotating sample stage for X-μCT scans. For each tomographic scan,
148 1261 X-ray projections were acquired with a constant angular step over a 360° rotation. The effective
149 pixel size of the images varied between 2.19 and 2.83 μm for a sample-to-detector distance between 8

and 54 mm. A maximum beam energy of 70 keV was used for most of the olivine scans but was set at 40 or 50keV for some rare crystals showing more beam artifacts (all conditions are reported in supplementary material). 3D reconstructions were done iteratively (e.g., adjustment of beam hardening, filter smooth). The images were imported in the ImageJ software to improve the contrast and brightness. For each scan, a brightness threshold is attributed for each phase (olivine, spinel, melt and vapour) in the Avizo™ software. Each image is then checked individually for additional segmentation corrections. After segmentation, melt and vapour renderings were smoothed during the surface reconstruction process using the filter packages in Avizo™ software. Textural measurements (size and volume) of the different phases (olivine, melt inclusions, vapor bubbles, spinels) were done using the Avizo™ software. The accuracy of the X-µCT technique to retrieve the phase volume (and number) is higher than classical techniques using point counting in transmitted light on 2D petrographic thin sections. For instance, most olivine crystals in a typical thin section are off-center intersected (Shea et al., 2015), and so measurements from thin sections generally underestimate the actual maximum dimensions of the crystals and their numbers.

2.3. Numerical modeling

Next, we aimed to use morphological constraints gleaned from 3D scans of natural olivine to investigate the influence of olivine morphology on rates of crystal settling in a basaltic melt. We simulated the flow of melt around crystals numerically, using morphologies representative of the range observed in 3D scans.

The equation of motion of a crystal suspended in melt (Carrara et al. 2019) may be written as:

$$\frac{dv}{dt} = \frac{\Delta\rho}{\rho_c}\boldsymbol{g} - \frac{\boldsymbol{F_D}}{m} \qquad (1)$$

where ρ_c is the density of the crystal, $\Delta\rho$ is the density contrast between the crystal and the surrounding melt ($\Delta\rho=\rho_c-\rho_l$, ρ_l being the density of the melt), $\boldsymbol{g}$ is the gravitational acceleration vector, m is the mass of the crystal, and the drag force imposed by the melt on the crystal $\boldsymbol{F_D}$. On the right-hand side of Eq. (1), the first term comprises both the gravitational and Archimedes' forces (reduced weight), while the second term corresponds to the drag force imposed by the melt on the crystal, $\boldsymbol{F_D}$ divided by the crystal mass. The drag force can be further decomposed as the product of that of an isolated crystal and a voidage function (Di Felice, 1994):

$$\boldsymbol{F_D} = \boldsymbol{F_{D,0}} f(\phi) \quad (2)$$

with $\boldsymbol{F_{D,0}}$ the drag force of an isolated crystal and ϕ the voidage function defined as:

$$f(\phi) = (1-\phi)^{-\beta} \quad (3)$$

where ϕ is the solid volume fraction around an isolated crystal, and β is the coefficient of momentum exchange between the crystal and the melt (β increases with crystal size and particle volume fraction; see supplementary material). The coefficient of momentum exchange can be further decomposed as (Di Felice, 1994):

$$\beta = 3.7 - 0.65 \exp\left(-\frac{[1.5 - log_{10}(\mathrm{Re})]^2}{2}\right) \quad (4)$$

which gives the following expression for the drag force:

$$\boldsymbol{F_D} = \boldsymbol{F_{D,0}}(1-\phi)^{-\left(3.7-0.65e^{\frac{-(1.5-log_{10}\mathrm{Re})^2}{2}}\right)} \quad (5)$$

where *Re* is the particle Reynolds number. β_0 depends on the viscosity and density of the melt, and the shape, size, and orientation of the crystal. The second part of the right-hand side of Eq. (5) is a correction that depends on the solid volume fraction (Di Felice, 1994). The particle Reynolds number (He and Tafti, 2018) is:

$$Re = \frac{d_{eq}\|\boldsymbol{v}-\boldsymbol{u}\|\rho_l}{\eta} \quad (6)$$

where d_{eq} is the diameter of a sphere having the same volume as the crystal, and η is the dynamic viscosity of the melt.

For the conditions relevant to crystals settling in melt, *Re* < 0.1, such that Eq. (5) can be simplified as:

$$\boldsymbol{F_D} = \boldsymbol{F_{D,0}}(1-\phi)^{-3.7} \quad (7)$$

The influence of the shape and orientation of the crystal on $\boldsymbol{F_{D,0}}$ may be isolated from the influence of its size and properties on the liquid phase by expressing it as a function of the drag coefficient, C_D (Zastawny et al. 2012; Sanjeevi et al. 2018):

$$\boldsymbol{F_{D,0}} = \frac{1}{2} C_D A \rho_l |v-u|(\boldsymbol{v}-\boldsymbol{u}) \quad (8)$$

with A representing the cross-sectional area of the crystal, $\boldsymbol{u}$ is the velocity vector of the melt, $\boldsymbol{v}$ is the velocity vector of the crystal. The drag force of an isolated crystal for which the cross-sectional area is assumed to be that of an equivalent sphere of diameter d_{eq} such that A = $\frac{\pi}{4} {d_{eq}}^2$ is defined as:

$$\boldsymbol{F_{D,0}} = \frac{\pi}{8} C_D \rho_l {d_{eq}}^2 |v-u|(\boldsymbol{v}-\boldsymbol{u}) \quad (9)$$

206 C_D depends on the density and viscosity of the liquid, the size of the particle, the shape of the particle,
207 and on the relative velocity between the flow and the particle. In the viscous regime, when Re<1 (almost
208 always the case for magmas), C_D is proportional to Re^{-1} (Sanjeevi et al. 2018) and is expressed as:

209 $$C_D = \frac{\xi}{Re} \qquad (10)$$

210 where ξ is a coefficient that depends on the shape and orientation of the particle. When the crystal
211 reaches its terminal settling velocity, U_T, the drag force equals the reduced weight of the particles such
212 as:

213 $$\frac{\Delta\rho}{\rho_c}\boldsymbol{g} = \frac{\boldsymbol{F_D}}{m} \qquad (11)$$

214 Inserting Eqs. 7 & 9 into Eq. (11) gives:

215 $$\frac{\Delta\rho}{\rho_c}\boldsymbol{g} = \frac{\pi C_D \rho_l {d_{eq}}^2 (1-\phi)^{-3.7} |\boldsymbol{v}-\boldsymbol{u}|(\boldsymbol{v}-\boldsymbol{u})}{8m} \qquad (12)$$

216 Inserting Eqs. (6 & 10) into Eq. (12):

217 $$\frac{\Delta\rho}{\rho_c}\boldsymbol{g} = \frac{\pi\xi\eta d_{eq}(1-\phi)^{-3.7}}{8m} U_T \qquad (13)$$

218 which gives the following expression for U_T after balancing the forces:

219 $$U_T = \frac{8\Delta\rho \boldsymbol{g} m}{\pi\xi\rho_c\eta d_{eq}(1-\phi)^{-3.7}} \qquad (14)$$

220 where g is the magnitude of $\boldsymbol{g}$. Increasing the crystal volume fraction decreases the permeability of the
221 suspension and increases the velocity and tortuosity of the flow of liquid in the intergranular spaces,
222 which in turn increases the drag force and decreases the settling velocity (Carrara et al., 2019).
223 To determine the shape and orientation factor, ξ, we conducted numerical simulations of the flow of the
224 melt around the crystal and computed the total force applied by the melt on the surface of the crystal.
225 We simulated the flow of melt around single crystals using the software MIGFLOW (Constant et al.,
226 2018), which solves the Navier-Stokes equations for an incompressible liquid employing a finite element
227 method. To generate a tetrahedral mesh around the crystal, we employed the software GMSH
228 (Geuzaine and Remacle, 2009). The computational domain is rectangular with the crystal located at its
229 center (Fig. 2a). The melt is injected at the base of the domain at constant velocity, U_{inj}, and can flow
230 outside the domain thanks to an outflow at constant pressure located atop. The sides of the domain are
231 free-slip walls and the surface of the crystal is a non-slip wall. Simulations are performed with no gravity
232 so that the force generated by the hydrostatic pressure gradient (i.e., the Archimedes' force) is null and
233 does not influence the estimation of ξ.

We computed the total drag force applied to the crystal by the melt, $\boldsymbol{F_D}$, by summing the contributions of the liquid force on all the element faces located at the surface of the crystal (Fig. 2b). The integration of the total drag force may be written as (Zastawny et al. 2012):

$$\boldsymbol{F_D} = \int_S (-p\boldsymbol{n_s} + \tau)\, dS \qquad (15)$$

where p is the melt pressure at the surface of the crystal (initially equal to 0), τ is the viscous stress tensor, $\boldsymbol{n_s}$ is the outward-pointing normal vector of the surface of the crystal, and dS is the incremental area. p is positive on the surface facing the flow and is negative on the faces on the other side of the crystal. The viscous stress is calculated as:

$$\tau = \eta \frac{\partial \boldsymbol{u^t}}{\partial \boldsymbol{n_s}} \qquad (16)$$

where $\boldsymbol{u^t}$ is the tangential velocity of the melt to the surface of the crystal, and $\partial \boldsymbol{u^t}/\partial \boldsymbol{n_s}$ is the gradient of the tangential velocity along $\boldsymbol{n_s}$. The shape and orientation factor of the isolated crystal is then calculated using a combination of Eq. (9) and Eq. (10):

$$\xi = \frac{8|F_D|}{\pi \eta d_{eq} U_{inj}} \qquad (17)$$

Three different characteristic olivine morphologies were tested, with variable aspect ratios along the three crystallographic axes: *a*- and *c*-elongated crystals, as well as an equant crystal. The choice of these morphologies is partly based on previous experimental studies and natural olivine crystals (Donaldson, 1976; Welsch et al., 2013; Mourey and Shea, 2019; Gordeychik et al., 2020), including those imaged in this study. All the crystal geometries were generated using MATLAB and have the same volume (~4.19 mm^3, which is equivalent to a 1-mm radius sphere). For each crystal morphology, we performed three simulations with one of the crystallographic axes aligned with the flow direction of the melt. For all the simulations and computations of settling velocity, we used the same physical properties for the melt and crystal (see Table 1). The ability of the numerical model to constrain settling velocities was validated by comparing the terminal velocity of a sphere using our numerical model and using the Stokes velocity (relative error of 0.89%; see supplementary material).

3. Results

3.1. 3D textures of Keanakāko‘i Tephra olivine

The Keanakāko‘i Tephra (unit K1) contains a large variety of olivine morphologies (Table 2 and Fig.3), which were classified in three morphological populations:

(1) Clustered polyhedral crystals are elongated along the *a*- or *c*-axis (4 clusters analyzed) and have the largest olivine grains (>2 mm; Fig. 3a). The complex morphology of these crystals is evaluated using the surface-area to volume (SA:V) ratio, measured by Avizo^{TM}. Clustered polyhedral crystals have low SA:V values between 1 mm^{-1} and 2 mm^{-1}. The clusters analyzed consist in 4 to 7 principal olivine phenocrysts (>500 μm), with up to 20 additional microphenocrysts- to microlite-sized crystals. Individual phenocrysts within polyhedral clusters have a more equant shape (relative to the other crystal morphologies discussed below) and large SA:V ratios (up to 20 mm^{-1}).

(2) Clustered skeletal crystals (2 clusters analyzed; Fig. 3b) are elongated along the *a*-axis and connected by melt inclusions that typically track the direction of primary and secondary growth branches (Fig. 3b). These crystals have high SA:V ratios between 7 mm^{-1} and 14 mm^{-1}. Spinel inclusions are concentrated near the olivine crystal edges. The crystal morphology and the abundance of melt inclusions suggests that clustered skeletal olivine formed at moderate-to-high undercooling conditions (i.e., -ΔT = 40-60°C; Mourey and Shea, 2019).

(3) Single skeletal crystals (7 crystals analyzed) are generally elongated along the *a*-axis (Fig. 3c). They are characterized by small, elongated melt inclusions (<50 μm) that are fully enclosed and not connected to vapor bubbles. Larger melt inclusions (up to 400 μm) usually form a tubular melt network that wraps vapor bubbles from both sides of the olivine crystals and may be open to the olivine surface (Fig. 3c). Spinel inclusions are only observed near the crystal edges. These crystals have medium SA:V values between 2 mm^{-1} and 6 mm^{-1}. Similar to the clustered skeletal crystals, single skeletal crystals likely formed at moderate-to-high undercooling conditions (i.e., -ΔT = 40-60°C).

3.1.1. Volume of melt, vapor bubble and spinel inclusions

The volume fraction of melt inclusions (reported in the supplementary material) varies from 3.6 to 22.1 vol.% in the single and clustered skeletal crystals (Fig. 4), but it is much smaller in the polyhedral clusters (between 0.45 and 1.4 vol.%; Fig. 4). Spinel makes up 0.3 - 1.4 vol.% of the total crystal volume. It is mostly located on the edges of skeletal crystals, and in both the cores and rims of polyhedral clusters (Fig. 3a). The volume occupied by vapor bubbles is usually low in polyhedral crystals (0 to 0.15 vol.%), medium in skeletal clusters (1.1 to 1.8 vol.%) and highly variable in single skeletal olivine crystals (0.24 to 4.8 vol.%). The vapor bubbles are generally attached to melt

inclusions (but some small bubbles are isolated as fluid inclusions as in k1820-ol8A; see supplementary material). Spinel, melt and vapor bubble inclusions modify the density of individual crystals in polyhedral clusters by < 0.5 % (Table 2; see supplementary material for detailed calculations). These inclusions affect the density of skeletal crystals (single or clusters) to a larger extent (up to 6% less dense). In the next sections, we compare the dimensions of the inclusions (spinel, vapor bubble, melt) of the different olivine crystal morphologies.

3.1.2. Size distributions of melt, vapor bubble and spinel inclusions

For ease of reporting and discussion, we express the size of individual objects (melt inclusions, spinels, vapor bubbles) as the diameter of a volume-equivalent sphere (d_{eq}).

The morphology of olivine-hosted melt inclusions is different in the three olivine types, suggesting variable magmatic conditions (or growth rates) for their formation and/or maturation. The size of melt inclusions (most of which are fully enclosed) in single skeletal olivine is highly heterogeneous (Fig. 5a). The largest melt inclusions in single skeletal olivine vary from d_{eq}<5 µm to d_{eq}=415 µm. As discussed in previous studies (Faure and Schiano, 2005; Mourey and Shea, 2019; Wallace et al., 2021), small melt inclusions may be inherited from larger inclusions that were split during crystal maturation and closing in of the skeletal framework. Melt inclusions in clustered olivine crystals are for the most part highly segregated (and highly oblate), with d_{eq}<100 µm (on average, d_{eq}=29 µm). Melt inclusions in the clustered olivine are equant, slightly larger than those in the skeletal crystals (d_{eq} < 200 µm, d_{eq} = 46 µm in average).

Vapor bubbles are usually connected to melt inclusions in clustered and single skeletal olivine crystals. Bubbles in clustered, *c*-elongated crystals are not common. They can be associated with melt inclusions or isolated as fluid inclusions (Fig. 3). The largest vapor bubbles (on average d_{eq} = 56 µm; maximum d_{eq} = 275 µm) are observed in single skeletal olivine crystals elongated along the *a*-axis (Fig. 5b). Smaller bubbles are present in clustered skeletal (d_{eq} = 44 µm average size) and c-elongated olivine clusters (d_{eq} = 27 µm average size).

Most spinel crystals are completely enclosed within their host olivine, or in some cases, partially exposed at the olivine surface. Their average and maximum sizes vary between the three olivine morphologies (Fig. 5c). In clustered and single skeletal crystals, they are generally smaller (d_{eq}= 9 ± 2 µm and maximum at d_{eq}=40-50 µm). In the polyhedral clusters dominated by c-elongated olivine

crystals, spinel crystals are on average larger (d_{eq}=15 µm) with some well faceted microphenocrysts (up to d_{eq}=170 µm; e.g., k1820-13A or k1820-5B). It is not possible to detect spinels smaller than ~2 µm (voxel resolution) using X-µCT scans or objects smaller than 8 µm^3. The number density of spinel is low in polyhedral crystal clusters (128 to 2,093 spinels /mm^3, or 405 to 3,184 spinels/cluster; Fig. 5d), medium-high in skeletal crystal clusters (3,461 and 4,289 spinel /mm^3, or 448 to 627 spinels/cluster), and highly variable for the single skeletal crystals (1,953 to 17,736 spinel /mm^3, or 106 to 2,093 spinels/crystal). Spinel size and volume in single and clustered skeletal crystals overlap with those of polyhedral crystal clusters (*c*-elongated, more mature crystals; Mourey and Shea, 2019). The volume of Cr-spinel observed in the olivine is likely related to the kinetics of olivine growth but through the mechanism is not yet understood. Welsch et al. (2013) proposed that Cr enrichments formed around rapidly growing olivine as Cr behaved incompatibly, leading to the crystallization of Cr-spinel that are later progressively buried in the inner part of the olivine crystal during slower growth. However, Cr generally shows partitionless or compatible behavior in the olivine-basalt system (Schreiber 1979; Lang et al. 2022) and therefore cannot easily pile up during rapid growth. It is possible that Cr-spinel simply forms prior to olivine and gets incorporated during rapid or slow growth (e.g., Roeder et al. 2006). The variation in the number density of spinel in the crystal may be related to changed in growth kinetics but further experiments are required to elucidate the exact mechanism through which Cr-spinel is included in olivine, often in high numbers.

Overall, the crystals scanned by X-µCT highlight the negligible effect of inclusions (melt/fluid, vapor bubble, Cr-spinel) on crystal settling (inclusions have little contribution to the particle density). Next, we leverage the morphologies identified in the 3D scans to define initial olivine crystal meshes that are integrated into numerical simulations (see section 2.3.). These simulations explore the influence of crystal shape and its orientation respective to the flow direction of the melt on the settling velocities.

3.2. Settling velocities

The results of the simulations are reported in terms of the coefficients of momentum exchange and settling velocities (Table 3) in the absence of other crystal (i.e., clusters). Figure 6 displays the evolution of the terminal velocity as a function of the solid volume fraction computed with Eq. (10) for all the orientations we simulated. In the context of a shear flow at low volume fraction, crystals tend to align

along the streamlines. At intermediate crystal volume fractions, the contacts between the crystals disturb this alignment and generate bimodal distributions of the shape-preferred direction (Arbaret et al., 2007). The preferential orientation of the crystals along their elongation direction compared to the melt flow minimizes friction with the melt and leads to an increase in the crystal's settling velocity. Overall, increasing the aspect ratio of a crystal tends to exacerbate the influence of its orientation on the settling velocity (Schwindinger and Anderson, 1989).

For the two non-equant crystals (elongated parallel to *a*- and *c*-axis; Fig. 2), the settling velocity is the highest when the long axis is parallel to the flow of the melt, and the lowest when the short axis is oriented in the flow direction. For the *a*-elongated crystal, the gap between the two lowest settling velocities (runs A2 and A3 in Fig. 6) is significant because the difference between the lengths of the short and intermediate axes (*b*-axis < *c*-axis) affects the projected areas of the crystal in the direction of the flow. The projected area is largest when the flow is along the *b*-axis (see a-elongated olivine in Fig. 2) and the settling velocity at a minimum (Fig. 6). This is illustrated by the larger contribution of the pressure component of the drag force in run A3 (~50% of the total drag force; Table 3) compared to the other simulations. On the contrary, the olivine elongated along the *c*-axis has its short and intermediate axes with similar lengths, such that the projected areas and settling velocities are more similar when the flow is aligned along the *a*-axis or *b*-axis (runs B1 and B2). The projected area of the crystal in the direction of the flow is, however, a bit larger when the a-axis is aligned with the flow, as illustrated by the larger contribution of the pressure component to the total drag force in run B1 (Table 3). The effect of the larger projected area on the settling velocity is balanced by the influence of the crystal morphology, which is more protruding along the *a*-axis than the *b*-axis (Fig. 2c). This makes the crystal more hydrodynamic along the a-axis than the *b*-axis, balancing the influence of the projected area and resulting in comparable settling velocities.

For the equant crystal, the difference between the settling velocities is controlled by the morphology of the surface of the crystal. The projected area of the crystal is the largest when the flow is along the *b*-axis, resulting in a lower settling velocity (Fig. 6) and a larger contribution of the pressure component to the total drag force (Table 3). The crystal has almost the same projected area when the flow is aligned along the *a*-axis or *c*-axis. The difference between the two settling velocities in these orientations results from the morphology of the crystal, which is more protruding along the *a*-axis.

To summarize, the simulations showed that the settling velocity is highest when the long axis of the crystal is aligned with the flow direction of the melt. Settling velocity decreases with the increasing aspect ratio of the crystal and leads to an increase in the influence of the crystal orientation (with the flow direction) on the terminal velocity. Based on these simulations, we find relatively high crystal settling rates (U_T) of ~9.7 x 10^{-6} to 1.4 x 10^{-5} m/s (or 3.5 to 5.0 cm/hour) for particle volume fractions (Φ) of 0 to 0.5. The complex olivine geometries decrease by factors of 3 to 5 the settling rates to that of ideal spheres with the same diameter ($\hat{U}_T$; Fig. 6). Overall, our estimated settling rates are more refined than previous Stockes velocities for Kilauea olivine (6.5 x 10^{-8} m/s to 4 x 10^{-5} m/s; Schwindinger 1999). In the following sections, we exploit our new settling rate estimates to constrain the timescales for the formation of olivine cumulates in mafic magma reservoirs. Then, we consider how crystal suspension times in magmatic reservoirs may affect real crystal size distribution (CSD) measured in Kīlauea samples.

4. Discussion

4.1. Suspension time of olivine crystals in basaltic melts

In this section, we evaluate the timescales over which olivine crystals can stay in suspension in a basaltic melt. We term this timescale the suspension time. We consider olivine crystals with realistic morphologies that undergo vigorous melt convection following an updated version of the model of Martin and Nokes (1988). This model considers a suspension of particles convecting within a viscous liquid of a given volume. A rheologically-locked layer, where the frictional contacts between the crystals oppose motion (Huber et al., 2010) is located at the base of the convecting volume (Fig.7a). Martin & Nokes (1988) model is valid at the base of the fluid where the convective velocity is zero, presumably meaning that that fluid thickness must be rather small. However, their model holds to a very good approximation even when the settling velocity is comparable to the convective velocity over the whole depth of the fluid. Therefore, we consider a convective layer of relatively small thickness (i.e. 200 m; Fig.7a) representative of the inferred size of most of Hawaiian sills (Ryan et al., 1983). The evolution of the number of particles located within the convective volume, *N*, is calculated using Eq. (6) of Martin and Nokes (1988):

$$\frac{dN}{dt} = \frac{-U_T}{h} N \qquad (18)$$

where U_T is the terminal settling velocity, and h is the height of the convective layer. Considering all the crystals as having the same volume, the number of particles within the convective layer, V_c, can be expressed as a function of ϕ:

$$N = \frac{\phi V}{V_c} \quad (19)$$

where V is the total volume of the convective layer (considered constant). Inserting Eq. (19) into Eq.(18) and neglecting the growth or dissolution of crystals (V_c constant) gives:

$$\frac{d\phi}{dt} = \frac{-U_T}{h}\phi \quad (20)$$

Inserting Eq. (9) into Eq. (20) gives the following differential equation describing the evolution of ϕ in the convective layer:

$$\frac{d\phi}{dt} = \frac{-\Delta\rho g m \phi}{h\rho_c \boldsymbol{F_{D,0}}(1-\phi)^{-3.7}} \quad (21)$$

To compare our model to that of Martin and Nokes (1988), we consider a convective layer with a height of 200 m with an initial particle volume fraction ϕ_0 = 0.5. We considered a dilute regime (where particle volume fractions in suspension represent <1 vol.%) and an intermediate regime (with particle volume fractions between 1-50 vol.%) but did not considered concentrated regimes where particle volume fractions is close to the maximum packing and where crystal-crystal interactions become important for the overall effective viscosity, the mobility of magmas and decrease magma convection (Bachmann and Bergantz, 2004; Faroughi and Huber, 2023). The coefficient of momentum exchange and terminal velocity used as input for the models are taken from the result of the 9 numerical simulations (Table 3). Unlike the model of Martin and Nokes (1988), our calculations account for the dependence of crystal settling velocity on ϕ. Therefore, the suspension time of crystals in the convective layer is a function of the initial particle volume fraction (ϕ_0; Fig. 7).

We find that if the settling velocity is constant (with a settling velocity fixed at ϕ = 0, as predicted by Eq. 13), the suspension time tends to be underestimated (predicted by Eq. 20; Fig. 7) and the settling rate of the particles is overestimated in comparison with the Martin and Nokes (1988) model. We neglect the decrease of magma convection caused by the high fraction of particles (ϕ up to 0.5) that can decrease our suspension times and therefore we propose maximum estimates for the suspension times. Moreover, the model does not consider the reentrainment of some crystals near the interface on top of the convective layer after their settling. The volume fraction of particles in suspension ϕ decreases with time for a given reservoir height (Fig. 7). ϕ in the convecting layer reaches less than

0.1 after 3 to 4 years for a 200 m magma body. Crystal settling of most of the particles (ϕ close to 0) in a small reservoir (i.e., sill with a height of 200 m) is reached in around 5 years in all the simulations performed.

Magma mixing and the addition of gas bubbles in the magma leads to complications for the understanding of crystal settling in natural volcanic systems. In natural magmas, crystals and silicate melt are interacting with exsolved volatiles at shallow depths. Adding a supercritical fluid such as CO_2 bubbles increases the settling rate of crystals (Schwindinger, 1999). Magmas with initially low volatile contents at depths (i.e., 0.3 wt.% CO_2 at >1 kbars for Kīlauea) can exsolve large amounts of volatile at shallower depths (in our previous example, up to 35 vol.% at 50 bars (Holloway, 1977; Flowers, 1979; Silver et al., 1990; Dixon et al., 1995; Anderson, 1995; Schwindinger, 1999). The upward streaming of the gas, associated with an intruding MgO-rich melt, can initiate a lateral segregation of the crystals and enhance the sedimentation rate of the olivine crystals by a factor of 5-10 (Schwindinger, 1999). Therefore, our settling rate estimates should be viewed as minimum values. Considering the likely presence of exsolving volatiles in natural basaltic reservoirs, the suspension time of 1-mm crystals, similar to those modeled in this paper, are on the order of a few years even for large mafic reservoirs (>1 km thick).

4.2. Application to mafic systems and the formation of olivine mushy zones

Our crystal settling simulations can be used to constrain the timescales required for the formation of olivine cumulates in basaltic systems. One limitation in our numerical simulations is that we did not consider the lateral motion of crystals expected to occur in natural sills (DiBenedetto et al., 2020). Crystal settling timescales in such sills are assumed to be short, and therefore cumulates can form rapidly in layers where convection is not effective. Notwithstanding, our results have implications for interpreting the formation of mush systems in active magma reservoirs. In mafic systems like Kīlauea, the solidification rate of a magma reservoir depends on olivine nucleation, growth and settling rates. Recrystallization can also affect the differentiation of a solidifying reservoir. Settling rates of olivine crystals, and thereby the timescales to form olivine cumulates, can only be constrained with information about their 3D geometry and the respective proportions of each crystal morphology (e.g., same number of crystals elongated along *a*-, *b*-, and *c*-axis). Future work is needed to document the

3D morphology of olivine crystals in exposed olivine cumulates to access information about their formation.

The relatively short suspension times of olivine crystals in a convective layer (a few years depending on the crystal volume fraction and reservoir size) could explain why most Pele's hairs, tears, scoria and tephra collected from lava lakes are typically aphyric (e.g., Thornber et al., 2015). Lava lakes like those at Kīlauea produce occasionally glassy juvenile ejecta falling as Pele's hair and tears, and small clots of spatter on the rim of Halema'uma'u (Wilson et al., 2008), but never sample the large proportions (~14 vol.%; Clague and Denlinger, 1994) of olivine cumulates that are present beneath Kīlauea summit, aerial and submarine Rift Zones (Delaney et al., 1990; Johnson, 1995; Denlinger, 1997). One reason may be that olivine settling is fast and efficient, which could be enhanced by exsolved volatiles (Schwindinger 1999). We propose that a rapid increase in the proportion of locked crystals that are not convecting and are not reinjected into the convecting melt is responsible for the formation of olivine aggregates observed in Hawaiian and other basaltic volcanoes. An increase in magma supply rate (as recently observed during the 21st century at Kīlauea, ~0.2 km^3/yr; Poland et al., 2014) increases the amount of heat provided to the reservoir and in turn the vigor of the convection, and it can trigger the reentrainment of some crystals near the interface between the locked layer and the convective layer. However, Kīlauea olivine crystals in the inner part of the locked layer may be well compacted and possibly deformed (Clague and Denlinger, 1994) and therefore not easily unlocked. The preponderance of magma mixing at Kīlauea (Lynn et al., 2017; Mourey et al., 2023) also favors undercooling and heating of the existing magma (and its crystal cargo) that counterbalance the solidification of the resident magma.

Using previous estimates of the vertical extent of olivine cumulate mush piles at Kīlauea (~180–720 m with ~40% porosity; Wieser et al., 2019), the constraints on Kīlauea reservoir radius from interferometric synthetic aperture radar (~2-4 km by InSAR; Baker and Amelung, 2012), and for olivine crystals equivalent to a 1 mm-radius sphere (same volume as in our simulations), we can estimate that a locked layer of mush may contain about 2.2 x 10^{17} to 3.5 x 10^{18} crystals. The convective melt may in turn contain 1.6 x 10^{16} to 2.6 x 10^{17} crystals, assuming an olivine volume fraction of 0.05 (Thornber et al., 2015). The locked layer (or mush piles) therefore contains ~13times more crystals than the convecting layer. Using our olivine crystal settling rates (U_T = 7.5 x.10^{-6} to 1.1 x.10^{-5} m/s at ϕ = 0.05),

498 we can estimate that 5 vol.% of olivine crystals in the convecting layer can reach the bottom of the
499 180–720 m reservoir in ~6 months to 3 years (ignoring the influence of volatiles and possible lateral
500 segregation). Assuming continuous nucleation of olivine crystals in the magma column, we estimate
501 that olivine mush piles at Kīlauea can be formed in < 5 years. Suspension timescales for olivine
502 crystals are much shorter than crystal storage timescales retrieved from melt inclusion studies (e.g.,
503 scavenging of century-old primitive olivine crystals with new olivine cargo during the Maunaulu 1969-
504 1974 eruption; Wieser et al., 2019) and a negligeable fraction of the tholeiitic shield stage period at
505 Kīlauea Volcano (starting around 240 ka years ago; Garcia et al., 2017). The low crystal fraction in
506 Kīlauea summit lavas (up to 5 vol.%) therefore implies that most of olivine cargo that nucleated at the
507 summit is stored either at the bottom of the summit reservoirs or in the Rift Zones. The poor constraint
508 on the intensity of magma convection at Kīlauea potentially strongly increases our crystal suspension
509 times (longer suspension) in the case of a highly convective magma reservoir. Our model also
510 assumes homogeneous nucleation in the magma column and do not consider any preferential crystal
511 nucleation or the formation of crystal cluster by growth (branching or surface nucleation) or synneusis
512 (reorientation and attachment of the grains to minimize the surface energy) that could also increase
513 our crystal settling estimates (Culha et al., 2020).
514
515 **4.3. Application to CSD studies**
516 Our olivine settling rates can also be used to evaluate the time frames over which crystal size
517 distributions (CSD) produced by crystal nucleation, growth, and ripening can evolve by gravitational
518 settling in mafic reservoirs. For a fixed reservoir height (h) and terminal velocity (U_T), the suspension
519 time of olivine crystals is a function of the particle volume fraction ϕ (Fig. 8). For olivine spanning
520 diameters equivalent to phenocryst sizes observed at Kīlauea (250 μm to 8 mm; Vinet and Higgins,
521 2010, 2011; Mourey and Shea, 2019), the suspension times vary from <1 year to a few years for mm-
522 sized crystals, up to a few centuries for smaller phenocrysts (250 μm). For instance, the phenocryst
523 fraction (>250 μm) from CSDs extracted from samples of the Maunaulu 1969-1974 eruption (Vinet and
524 Higgins, 2010) correspond to suspension times ranging from ~6 months (for larger phenocrysts) to
525 ~120 years (for crystals close to 250 μm in size). Our calibration could therefore be used to re-interpret
526 CSDs from melt-dominated basaltic systems in terms of crystal suspension times.
527

Conclusion

We conducted X-μCT scans of olivine crystals from Kīlauea Volcano to elucidate the complexities of olivine internal textures. The crystal scans reveal complex melt, spinel and vapor bubble shapes, and a large diversity of inclusion volumes. We show that mineral, melt and gas inclusions only modify the density of crystals by up to 6% relative, which has a limited effect on crystal settling rates in comparison with the crystal shape. We thus explore the effect of crystal morphology on settling rate using numerical simulations. We find that the settling velocity is higher when the elongated crystallographic axis is aligned with the flow of the melt. We evaluate the time of the olivine crystals suspended in a reservoir undergoing vigorous convection. Suspension times vary with the initial particle volume fraction, but in general, olivine crystals have short (<5 years) suspension times in a convective layer. The short suspension times may in turn affects the rates of solidification at the base of a basaltic reservoir in synergy with magma cooling and crystallization. We also propose a calibration of olivine suspension times (based on known particle volume fraction, reservoir height, olivine morphology) that can be used to interpret the CSDs in terms of crystal suspension times in a mafic reservoir. Crystal settling is a potentially key melt differentiation mechanism, as has been highlighted at some ocean island volcanoes (e.g., Pankhurst et al., 2018a) but may also be of importance at other melt-dominated mafic volcanoes.

CRediT authorship contribution statement

Adrien J. Mourey: Conceptualization, Data curation, Formal analysis, Investigation, Methodology, Software, Visualization, Writing – original draft. **Alexandre Carrara:** Conceptualization, Funding acquisition, Investigation, Methodology, Software, Visualization, Writing – original draft, Writing – review & editing. **Thomas Shea**: Funding acquisition, Investigation, Methodology, Software, Writing – review & editing. **Fidel Costa:** Conceptualization, Funding acquisition, Writing – review & editing. **Marc-Antoine Longpré**: Conceptualization, Funding acquisition, Writing – review & editing.

Declaration of competing interest

The authors declare that they have no known competing financial interests or personal relationships that could have appeared to influence the work reported in this paper.

558

559 **Data availability**

560 All data obtained in this study are included in the supplementary data tables.

561

562 **Acknowledgments**

563 The authors thank Jessica Maisano at the NSF-supported UTCT facility for assistance with the
564 microtomography scans. A.M. and T.S. received funding from the National Science Foundation (NSF)
565 grant to T.S. (EAR 1725321). A.C. was partly supported by the National Science Foundation grant
566 EAR-1950113, and the Region Auvergne and the European Regional Development Fund (Laboratory
567 of Excellence ClerVolc contribution number XXX). M.-A.L. was supported through NSF award EAR
568 1650379. The authors thank the editor and the two reviewers (Jérémie Vasseur and Matt Pankhurst)
569 for their detailed evaluation of this manuscript and for the constructive set of comments.

570 **References**

571

572 Anderson, A.T., 1995. CO_2 and the eruptibility of picrite and komatiite. Lithos 34, 19–25.

573

574 Arbaret, L., Bystricky, M., Champallier, R., 2007. Microstructures and rheology of hydrous synthetic
575 magmatic suspensions deformed in torsion at high pressure. *J. Geophys. Res.: Solid Earth*, *112*(B10).

576

577 Arzilli, F., Agostini, C., Landi, P., Fortunati, A., Mancini, L., Carroll, M.R., 2015. Plagioclase nucleation
578 and growth kinetics in a hydrous basaltic melt by decompression experiments. Contrib. Mineral. Petrol.
579 170(5-6).

580

581 Bachmann, O., Bergantz, G. W., 2004. On the origin of crystal-poor rhyolites: extracted from
582 batholithic crystal mushes. J. Petrol. 45(8), 1565-1582.

583

584 Bachmann, O., Huber, C., 2019. The inner workings of crustal distillation columns; the physical
585 mechanisms and rates controlling phase separation in silicic magma reservoirs. *Journal of*
586 *Petrology*, *60*(1), 3-18.

587

588 Baker, S., Amelung, F., 2012. Top-down inflation and deflation at the summit of Kīlauea Volcano,
589 Hawai'i observed with InSAR. J. Geophys. Res. 117, 1–14.
590
591 Byron, D.N., Atherton, M.P., Hunter, R.H., 1995. The interpretation of granitic textures from serial thin
592 sectioning, image analysis and three-dimensional reconstruction. Mineral. Magazine 59, 203–211.
593
594 Carrara, A., Burgisser, A., & Bergantz, G. W. (2019). Lubrication effects on magmatic mush dynamics.
595 *Journal of Volcanology and Geothermal Research*, *380*, 19-30.
596
597 Clague, D.A., Denlinger, R.P., 1994. Role of olivine cumulates in destabilizing the flanks of Hawaiian
598 volcanoes. Bull. Volcanol. 56(6-7), 425–434.
599
600 Clark, A. H., Pearce, T. H., Roeder, P. L., Wolfson, I., 1986. Oscillatory zoning and other
601 microstructures in magmatic olivine and augite: Nomarski interference contrast observations on etched
602 polished surface. Am. Mineral. 71, 734–741.
603
604 Constant, M., Dubois, F., Lambrechts, J., Legat, V., 2018. Implementation of an unresolved stabilised
605 FEM–DEM model to solve immersed granular flows. Computational Particle Mechanics.
606
607 Culha, C., Suckale, J., Keller, T., & Qin, Z., 2020. Crystal fractionation by crystal-driven
608 convection. *Geophysical Research Letters*, *47*(4), e2019GL086784.
609
610 Daniel, C.G., Spear, F.S., 1999. The clustered nucleation and growth processes of garnet in regional
611 metamorphic rocks from north-west Connecticut, USA. J. Metam. Geol. 17, 503–520.
612
613 Delaney, P.T., Fiske, R.S., Miklius, A., Okamura, A.T., Sako, M.K., 1990. Deep Magma Body Beneath
614 the Summit and Rift Zones of Kilauea Volcano, Hawaii. Science 247(4948), 1311–1316.
615
616 Denlinger, R.P., 1997. A dynamic balance between magma supply and eruption rate at Kilauea
617 volcano, Hawaii. J. Geophys. Res.: Solid Earth 102(B8), 18091–18100.

DiBenedetto, M., Qin, Z., Suckale, J., 2020. Crystal aggregates record the pre-eruptive flow field in the volcanic conduit at Kīlauea, Hawaii. Sci. Adv. 6(49), eabd4850.

Di Felice, R., 1994. The voidage function for fluid-particle interaction systems. Inter. J. Multiphase Flow 20(1), 153–159.

Dixon, J.E., Stolper, E.M., Holloway, J.R., 1995. An experimental study of water and carbon dioxide solubilities in mid-ocean ridge basaltic liquids. Part I: Calibration and solubility models. J. Petrol. 36, 1607–1631.

Donaldson, C.H., 1976. An experimental investigation of olivine morphology. Contrib. Mineral. Petrol. 57, 187–213.

Elkins-Tanton, L.T., 2012. Magma Ocean in the inner solar system. Annu. Rev. Earth Planet. Sci. 40, 113–139.

Faroughi, S. A., Huber, C., 2023. Rheological state variables: A framework for viscosity parametrization in crystal-rich magmas. J. Volc. Geotherm. Res., 440, 107856.

Faure, F., Trolliard, G., Nicollet, C., Montel, J.-M., 2003. A developmental model of olivine morphology as a function of the cooling rate and the degree of undercooling. Contrib.Mineral. Petrol. 145, 251–263.

Faure, F., Schiano, P., 2005. Experimental investigation of equilibration conditions during forsterite growth and melt inclusion formation. Earth Planet Sci. Lett. 236, 882–898.

Flowers, G.C., 1979. Correction of Holloway's 1977. Adaptation of the modified Redlich–Kwong equation of state for calculation of the fugacities of molecular species in supercritical fluids of geologic interest. Contrib. Mineral. Petrol. 69, 315–318.

Garcia, M.O., Jicha, B.R., Marske, J.P., Pietruszka, A.J., 2017. How old is Kīlauea Volcano? Insights from $^{40}Ar/^{39}Ar$ dating of the 1.7-km-deep SOH-1 core. Geology 45, 79–82.

Geuzaine, C., Remacle, J.-F., 2009. Gmsh: A 3-D finite element mesh generator with built-in pre- and post-processing facilities. Inter. J. Num. Meth. Eng. 79(11), 1309–1331.

Giordano, D., Russell, J. K., & Dingwell, D. B. (2008). Viscosity of magmatic liquids: a model. *Earth and Planetary Science Letters*, *271*(1-4), 123-134.

Gordeychik, B., Churikova, T., Shea, T., Kronz, A., Simakin, A., Wörner, G., 2020. Fo and Ni relations in olivine differentiate between crystallization and diffusion trends. J. Petrol. 61, egaa083.

He, L., Tafti, D. K., & Nagendra, K. (2017). Evaluation of drag correlations using particle resolved simulations of spheres and ellipsoids in assembly. *Powder technology*, *313*, 332-343

Holloway, J.R., 1977. Fugacity and activity of molecular species in supercritial fluids. In: D.G. Fraser, Ed., Thermodynamics in Geology. Reidel Publishing, Dordrecht, Holland, 161–181.

Holness, M.B., Farr, R., Neufeld, J.A., 2017. Crystal settling and convection in the Shiant Isles Main Sill. Contrib. Mineral. Petrol. 172.

Huber, C., Bachmann, O., Dufek, J., 2010. The limitations of melting on the reactivation of silicic mushes. J. Volcanol. Geotherm. Res. 195(2-4), 97–105.

Jambon, A., Lussiez, P., Clocchiatti, R., Weisz, J., Hernandez, J., 1992. Olivine growth rates in a tholeiitic basalt; an experimental study of melt inclusions in plagioclase. Chem. Geol. 96, 277–287.

Johnson, D.J., 1995. Molten core model for Hawaiian rift zones. J. Volcanol. Geotherm. Res. 66(1-4), 27–35.

Koyaguchi, T., Hallworth, M., Huppert, H. et al., 1990. Sedimentation of particles from a convecting fluid. Nature 343, 447–450.

Lang, S., Mollo, S., France, L., Misiti, V., Nazzari, M., 2022. Partitioning of Ti, Al, P, and Cr between olivine and a tholeiitic basaltic melt: Insights on olivine zoning patterns and cation substitution reactions under variable cooling rate conditions. Chemical Geology, 601, 120870.

Lavorel, G., Le Bars, M., 2009. Sedimentation of particles in a vigorously convecting fluid. Phys. Rev. E 80, 046324.

Lynn, K.J., Garcia, M.O., Shea, T., Costa, F., Swanson, D.A., 2017. Timescales of mixing and storage for Keanakāko'i tephra magmas (1500–1820 CE), Kīlauea volcano, Hawai'i. Contrib. Mineral. Petrol. 172, 76-96.

Martin, D., Nokes, R., 1988. Crystal settling in a vigorously converting magma chamber. Nature 332, 534–536.

Mock, A., Jerram, D.A., 2005. Crystal size distribution (CSD) in three dimensions: insights from the 3D reconstruction of a highly porphyritic rhyolite. J. Petrol. 46, 1525–1541.

Mourey, A.J., Shea, T., 2019. Forming olivine phenocrysts in basalt: a 3D characterization of growth rates in laboratory experiments. Front. Earth Sci. 7.

Mourey, A.J., Shea, T., Lynn, K.J., Lerner, A.H., Lambart, S., Costa, F., Oalmann, J., Lopaka Lee, R., Gansecki, C., 2022. Trace elements in olivine fingerprint the source of 2018 magmas and shed light on explosive-effusive eruption cycles at Kīlauea Volcano. Earth Planet. Sci. Lett. 595, 117769

Mourey, A.J., Shea, T., Hammer, J.E., 2023. Preservation of magma recharge signatures in Kilauea olivine during protracted storage. J. Geophys. Res.: Solid Earth e2022JB025523. https:// doi. org/ 10.

1029/ 2022J B0255 23

Murata, K.J., Richter, D.H., 1966. The settling of olivine in Kilauean magma as shown by lavas of the 1959 eruption. Am. J. Sci. 264(3), 194–203.

Oppenheimer, J., Patel, K., Lindoo, A., Hillman, E.M.C., Lev, E., 2021. High-Speed 3D Imaging of Multiphase Systems: Applying SCAPE Microscopy to Analog Experiments in Volcanology and Earth Sciences. Geochem. Geophys. Geosyst. 22(3).

Pankhurst, M.J., Dobson, K.J., Morgan, D.J., Loughlin, S.C., Thordarson, T., Lee, P.D., Courtois, L., 2014. Monitoring the magmas fuelling volcanic eruptions in near-real-time using X-ray micro-computed tomography. J. Petrol. 55 (3), 671–684.

Pankhurst, M.J., Morgan, D.J., Thordarson, T., Loughlin, S.C., 2018a. Magmatic crystal records in time, space, and process, causatively linked with volcanic unrest. Earth Planet. Sci. Lett. 493, 231–241.

Pankhurst, M.J., Vo, N.T., Butcher, A.R., et al., 2018b. Quantitative measurement of olivine composition in three dimensions using helical-scan X-ray micro-tomography. Am. Mineral. 103(11), 1800–1811.

Pearce, T.H., 1984. The analysis of zoning in magmatic crystals with emphasis on olivine. Contrib. Mineral. Petrol. 86, 149–154.

Polacci, M., Baker, D.R., Mancini, L., Tromba, G., Zanini, F., 2006. Three-dimensional investigation of volcanic textures by X-ray microtomography and implications for conduit processes. Geophys. Res. Lett. 33(13).

Poland, M.P., Miklius, A., Montgomery-Brown, E.K., 2014. Magma supply, storage, and transport at shield-stage Hawaiian volcanoes. USGS Prof. Pap. 1801. pp.179–234.

738

739 Roeder, P., Gofton, E., Thornber, C., 2006. Cotectic proportions of olivine and spinel in olivine-
740 tholeiitic basalt and evaluation of pre-eruptive processes. Journal of Petrology, 47(5), 883-900.
741

742 Ryan, M.P., Blevins, J.Y.K., Okamura, A.T., Koyanagi, R.Y., 1983. Magma reservoir subsidence
743 mechanisms: Theoretical summary and application to Kilauea Volcano Hawaii. J. Geophys. Res. 88,
744 4147–4181.
745

746 Sanjeevi, S. K., Kuipers, J. A. M., & Padding, J. T., 2018. Drag, lift and torque correlations for non-
747 spherical particles from Stokes limit to high Reynolds numbers. *International Journal of Multiphase*
748 *Flow*, *106*, 325-337.
749

750 Schmidt, M.W., Forien, M., Solferino, G., Bagdassarov, N., 2012. Settling and compaction of olivine in
751 basaltic magmas: an experimental study on the time scales of cumulate formation. Contrib. Mineral.
752 Petrol. 164, 959-976.
753

754 Schreiber, H. D., 1979. Experimental studies of nickel and chromium partitioning into olivine from
755 synthetic basaltic melts. In: Lunar and Planetary Science Conference, 10th, Houston, Tex., March 19-
756 23, 1979, Proceedings. Volume 1.(A80-23557 08-91) New York, Pergamon Press, Inc., 1979, p. 509-
757 516. Research supported by the Research Corp.; (Vol. 10, pp. 509-516).
758

759 Schwindinger, K.R., Anderson, A.T, 1989. Synneusis of Kilauea Iki olivines. Contr. Mineral. And Petrol.
760 103, 187–198.
761

762 Schwindinger, K.R., 1999. Particle dynamics and aggregation of crystals in a magma chamber with
763 application to Kilauea Iki olivines. J. Volcanol. Geotherm. Res. 88(4), 209–238.
764

765 Shea, T., Costa, F., Krimer, D., Hammer, J.E., 2015. Accuracy of timescales retrieved from diffusion
766 modeling in olivine: a 3D perspective. Am. Mineral. 100, 2026–2042.
767

768 Silver, L.A., Ihinger, P.D., Stolper, E., 1990. The influence of bulk composition on the speciation of
769 water in silicate glasses. Contrib. Mineral. Petrol. 104, 142–162.
770
771 Solomatov, V., Olson, P., Stevenson, D., 1993a. Entrainment from a bed of particles by thermal
772 convection. Earth Planet. Sci. Lett. 120, 387.
773
774 Solomatov, V., Stevenson, D., 1993b. Suspension in convective layers and style of differentiation of a
775 terrestrial magma ocean. J. Geophys. Res. 98, 5375.
776
777 Swanson, D.A., Rose, T.R., Fiske, R.S., McGeehin, J.P., 2012. Keanakāko'i Tephra produced by 300
778 years of explosive eruptions following collapse of Kīlauea's caldera in about 1500 CE. J. Volcanol.
779 Geotherm. Res. 215–216:8–25.
780
781 Thornber, C.R., Orr, T.R., Heliker, C., Hoblitt, R.P., 2015. Petrologic testament to changes in shallow
782 magma storage and transport during 30+ years of recharge and eruption at Kīlauea Volcano, Hawai'i.
783 In: Carey, R.J., Cayol, V., Poland, M.P., Weis, D. (Eds.), Hawaiian Volcanoes: From Source to
784 Surface. Am. Geophys. Un. Geophys. Mono. 208, 147–188.
785
786 Vinet, N., Higgins, M. D., 2010. Magma solidification processes beneath Kilauea volcano, Hawaii: A
787 quantitative textural and geochemical study of the 1969–1974 Mauna Ulu Lavas. J. Petrol. 51(6),
788 1297-1332.
789
790 Vinet, N., Higgins, M. D., 2011. What can crystal size distributions and olivine compositions tell us
791 about magma solidification processes inside Kilauea Iki lava lake, Hawaii?. J. Volcanol. Geotherm.
792 Res. 208(3-4), 136-162.
793
794 Wallace, P.J., Plank, T., Bodnar, R.J., Gaetani, G.A., Shea, T., 2021. Olivine-hosted melt inclusions: a
795 microscopic perspective on a complex magmatic world. Ann. Rev. Earth Planet. Sci. 49
796

797 Welsch, B., Faure, F., Famin, V., Baronnet, A., Bachelery, P., 2013. Dendritic crystallization: a single
798 process for all the textures of olivine in basalts? J. Petrol. 54, 539–574.
799
800 Wieser, P.E., Edmonds, M., Maclennan, J. et al., 2019. Crystal scavenging from mush piles recorded
801 by melt inclusions. Nat. Commun. 10, 5797.
802
803 Wilson, D., Elias, T., Orr, T., Patrick, M., Sutton, J., Swanson, D., 2008. Small explosion from new vent
804 at Kilauea's summit. Eos Trans. AGU, 89, 203.
805
806 Zastawny, M., Mallouppas, G., Zhao, F., & Van Wachem, B. (2012). Derivation of drag and lift force
807 and torque coefficients for non-spherical particles in flows. *International Journal of Multiphase Flow*,
808 *39*, 227-239.

Fig. 1. Location of Kīlauea Volcano (left panel) and map of Kīlauea's summit (right panel). Background digital elevation model from August 2018, with the 2018 collapse area shaded in pink. Black cross represents coordinate system at 19.4073º N, 155.2784 º W. The location of the Golden Pumice eruption unit (Unit K1 from the explosive Keanakāko'i Tephra), the source of olivine phenocrysts used for this study, is indicated by the red star.

Fig. 2. Numerical simulations of olivine settling. (a) Numerical simulation of the flow of melt around an olivine crystal. The black box corresponds to the limit of the computational domain. The two gray surfaces represent the mass inflow and pressure outflow boundary conditions. The crystal is located at the center of the domain. The curves located within the domain are the melt flow streamlines color-coded for magnitude of flow velocity. (b) Zoom on the crystal. The red line indicates the edges of the particles. The mesh corresponds to the surface elements on which the force applied by the liquid is computed. (c) Geometry of the olivine crystals we have tested. Crystals used in the numerical simulations are either elongated along the *a*-axis, elongated along the *c*-axis or equant. The three crystal morphologies have the same volume ($\sim$ 4.19 mm^3) equivalent to a 2-mm sphere diameter.

824 **Fig. 3. Representative secondary electron images (in grey) and 3D renderings of olivine**
825 **crystals from the 1820 Keanakāko'i (unit K1) eruption.** (a) Clustered polyhedral olivine elongated
826 along the c-axis; (b) Clustered skeletal olivine elongated along the a-axis; (c) Skeletal olivine
827 elongated along the a-axis. Numbers in the pie charts are relative volume % of the different phases in
828 the crystal (melt inclusions, Cr-spinel, vapor bubbles) retrieved from the Avizo™ software. Note that
829 only inclusion fractions are represented in the pie charts (not the olivine fraction).
830

Fig. 4. Melt inclusion and vapor bubble relative volume % extracted from 3D renderings. Cr-spinel in olivine makes up <1.5 volume % in all cases.

834 **Fig. 5. Size of inclusions in olivine.** Distribution (illustrated as violin plots) of equivalent sphere
835 diameters of (a) melt inclusions, (b) vapor bubbles, (c) Cr-spinel crystals and (d) density of Cr-spinel /
836 mm^3) in skeletal crystal clusters, polyhedral crystal clusters and single skeletal olivine crystals
837 elongated along the *a*-axis. Cr-spinels are larger in polyhedral clusters (both the mean and maximum
838 diameter) than in skeletal clusters and skeletal single crystals. Most melt inclusions have an equivalent
839 sphere diameter <100 μm (segmented melt inclusions) but larger melt inclusions (up to 415 μm) are
840 also observed in skeletal olivine crystals elongated along the a-axis. The filled white circles indicate
841 the median value of the distribution, the filled grey areas are the interquartile ranges, and the thin
842 black lines represent the rest of the distribution.
843
844

Fig. 6. Variation of the settling velocity (U_T) of olivine crystals with particle volume fraction (ϕ) for different crystal geometries and orientation with respect to the melt flow direction. Inset: ratio of olivine settling rates with different geometries to that of ideal spheres with the same diameter ($\hat{U}_T$) as a function of ϕ ($\phi = 0$ for the Stokes' velocity). The highest speeds are those when the elongated crystal axis is aligned with the flow. Complex crystal geometries decrease settling rates by factors of 3 to 5 compared to spherical shapes.

852 **Fig. 7. Time evolution of the particle volume fraction (ϕ) in suspension in the convective melt**
853 **layer as a function of the crystal morphology.** (a) We consider a convective layer (in blue), in which
854 convection occurs and with particle volume fraction ϕ=*0-0.5*, and a locked layer (in red), in which no
855 convection occurs (with ϕ >0.5). The black circles represent the particles. The red arrows indicate the
856 convection. The green dashed line indicates the limit between the convective and locked domain. A
857 relatively small convective layer of 200 m is considered for the calculations since the fluid thickness
858 must be rather small for the Martin & Nokes (1988) model. (b) Suspension times (in years) of olivine
859 crystals in the convective layer as a function of the particle volume fraction (ϕ), the crystal morphology
860 (see the parameters for the simulations in Tables 1 & 3). The blue, red and black curves correspond
861 to the numerical solution of Eq. (20) for the different simulations.
862

Fig. 8. Effect of crystal size (d_{eq}) on suspension time and as a function of the particle volume fraction (ϕ). Only phenocryst sizes between 250 μm and 8 mm (in diameter) are displayed. The size of the reservoir (h) is fixed at 200 m for the calculations. The terminal velocity (U_T) is fixed at 1.36 x 10^{-5} m/s (olivine elongated along a-axis with the a-axis aligned with the flow, run A1 in Table 3). This calibration for the suspension timescales can be adapted for a given magmatic system with a known magma reservoir height and olivine morphology.

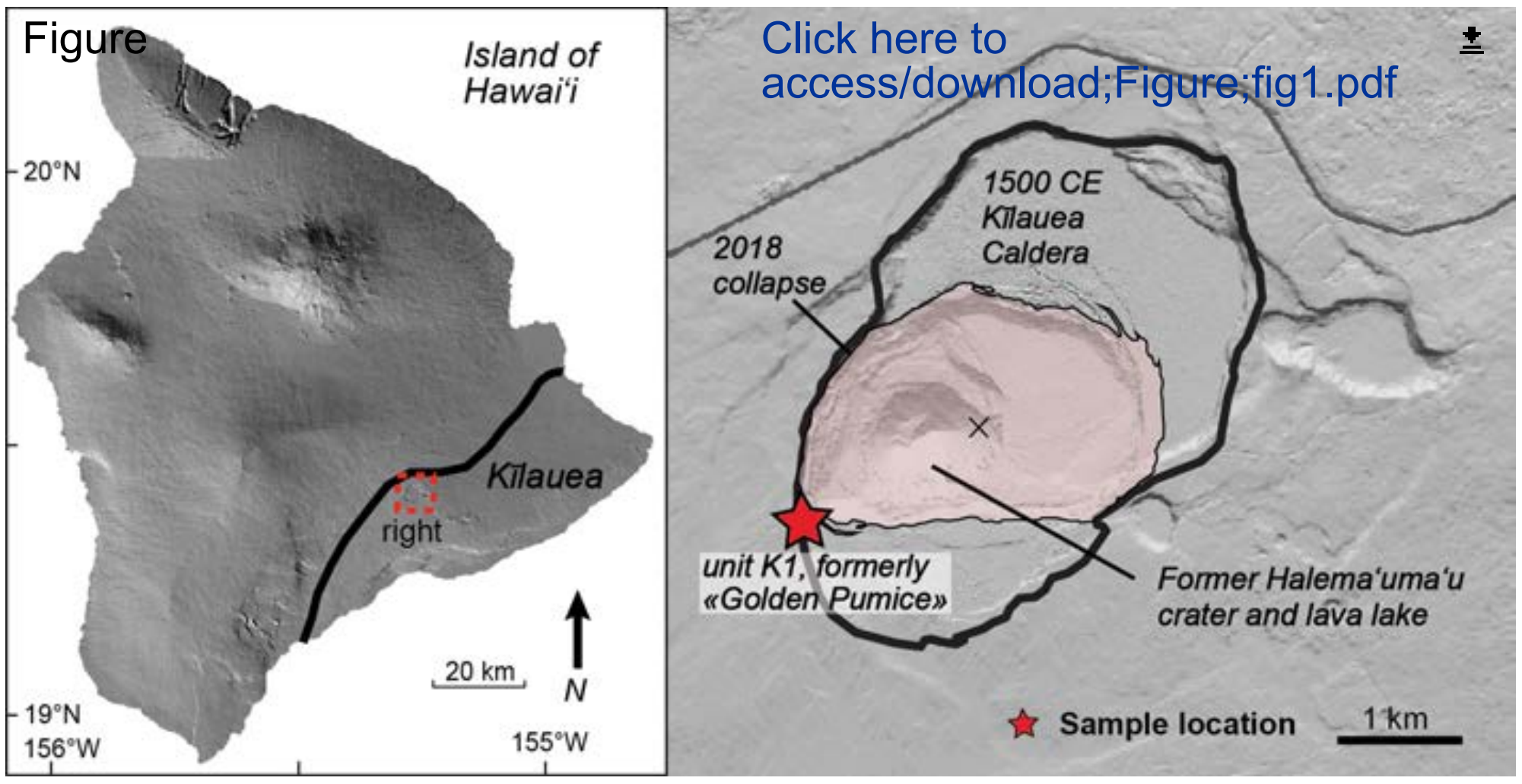
Figure
Island of Hawai'i
20°N
19°N
156°W
155°W
Kīlauea
right
20 km
N
Click here to access/download;Figure;fig1.pdf
1500 CE Kīlauea Caldera
2018 collapse
unit K1, formerly «Golden Pumice»
Former Halema'uma'u crater and lava lake
Sample location
1 km

Figure

Click here to access/download;Figure;fig2.pdf

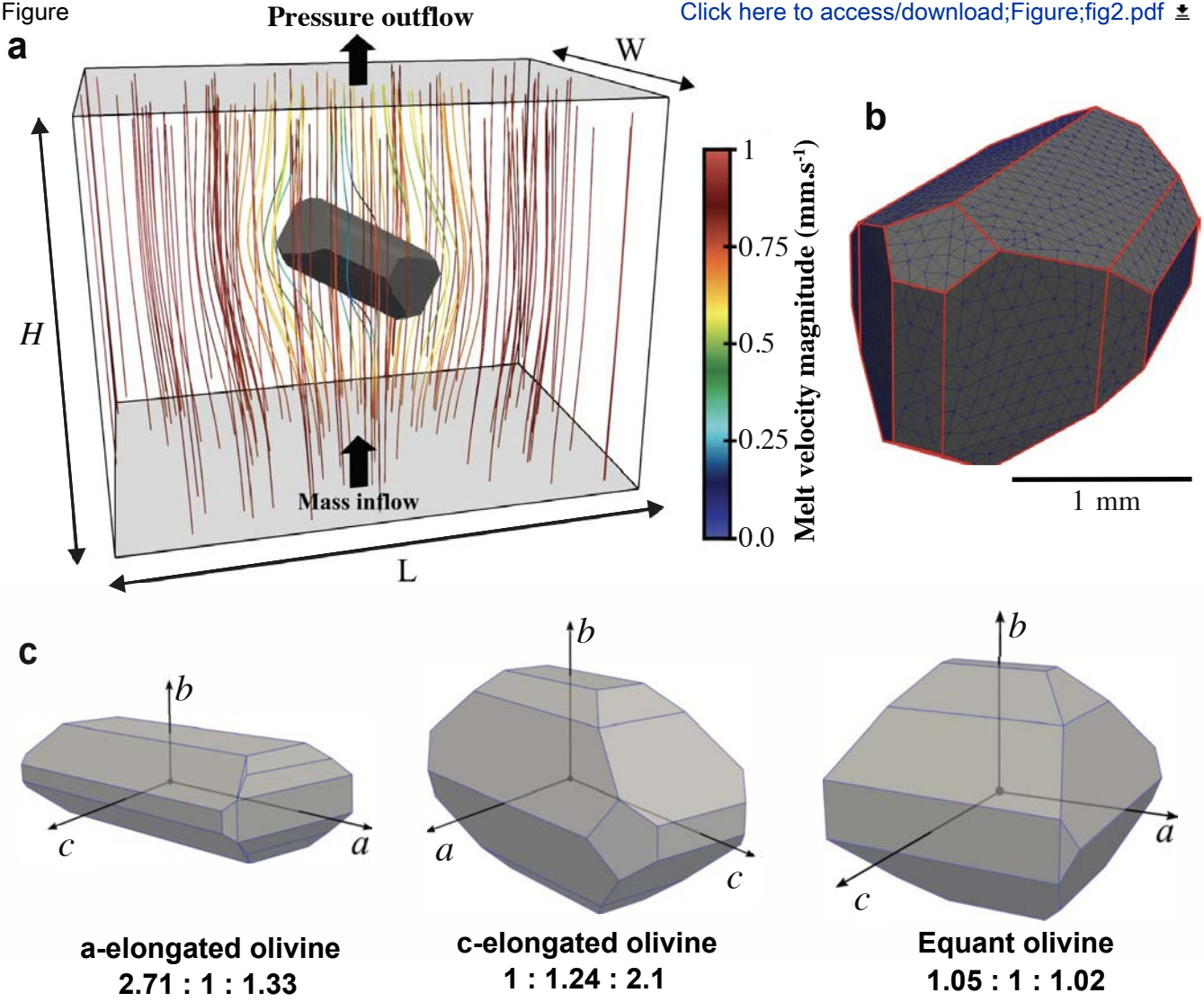

Figure

Legend for X-µCT scans

- Olivine
- Melt inclusions
- Cr-spinel
- Vapor bubble

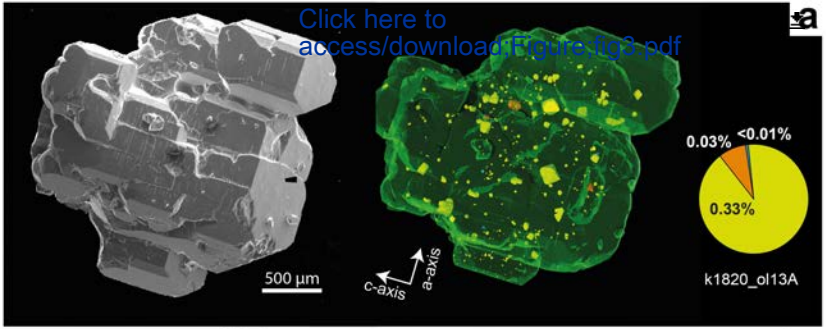

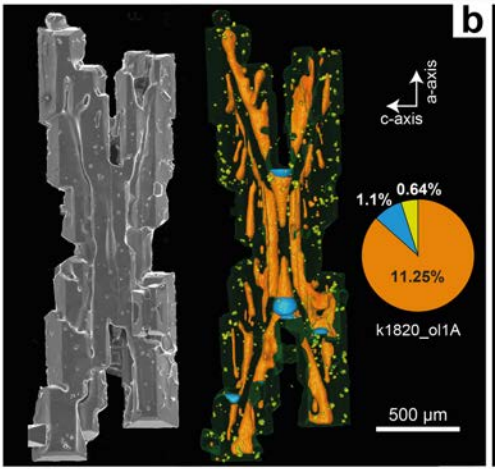

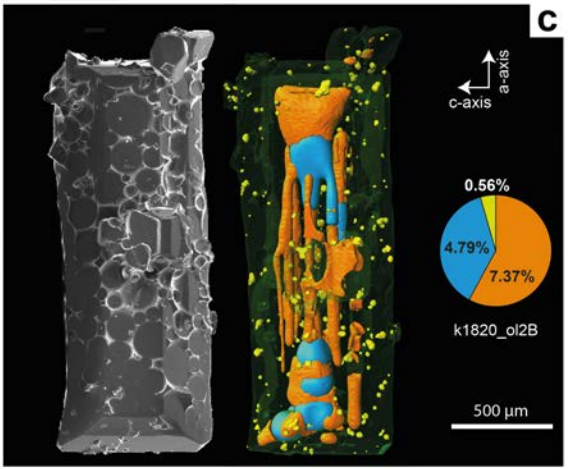

Figure

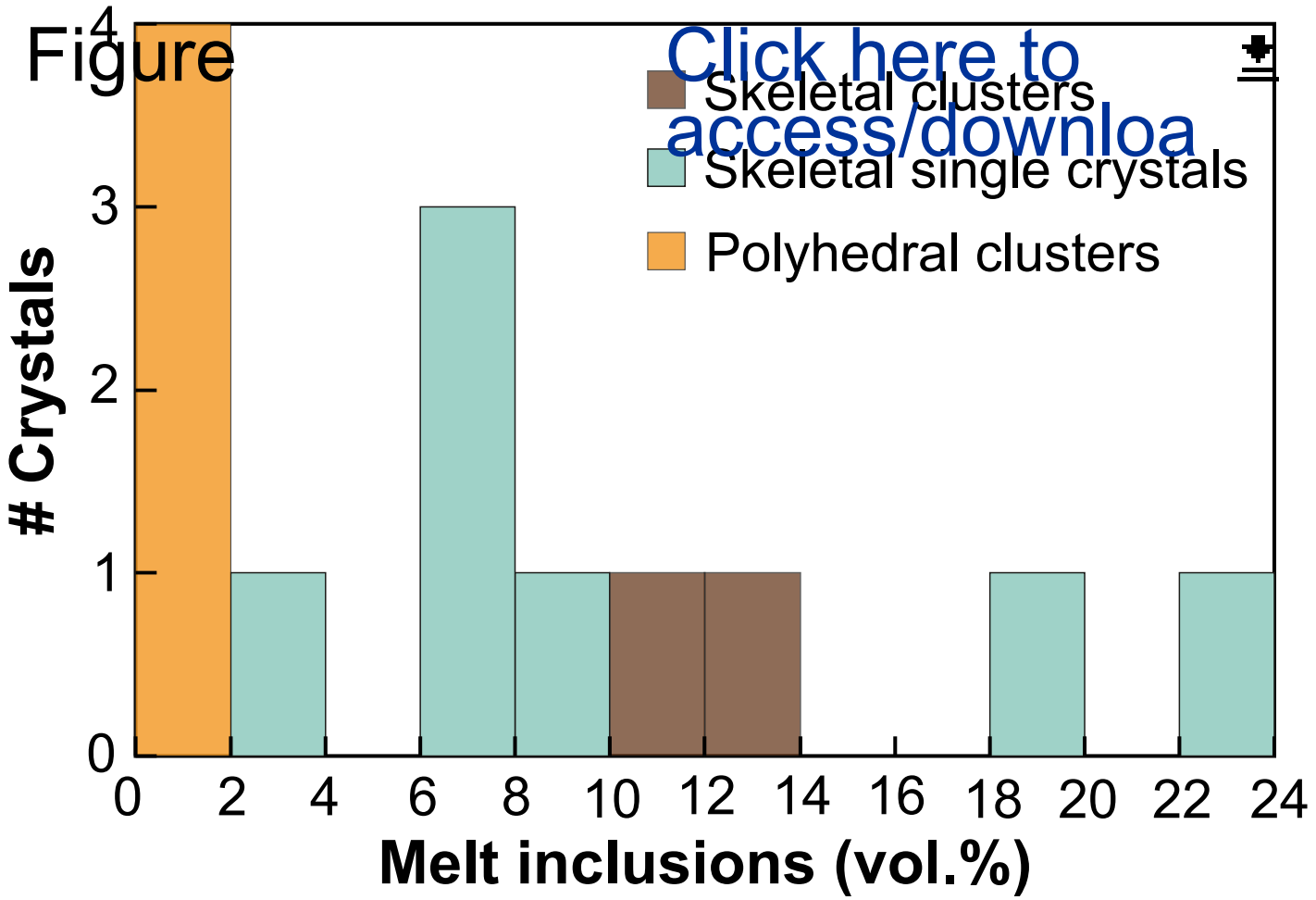

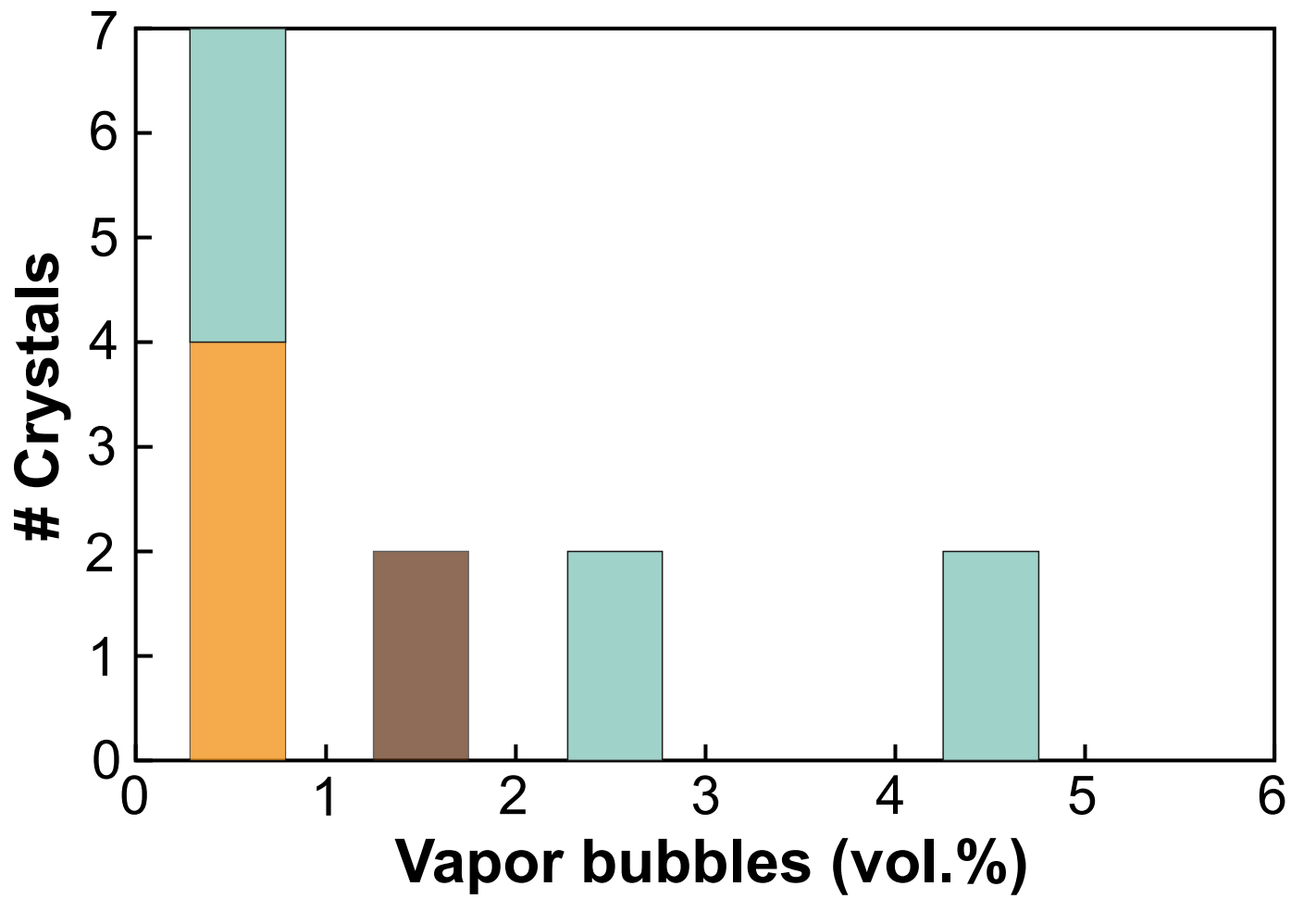

Figure

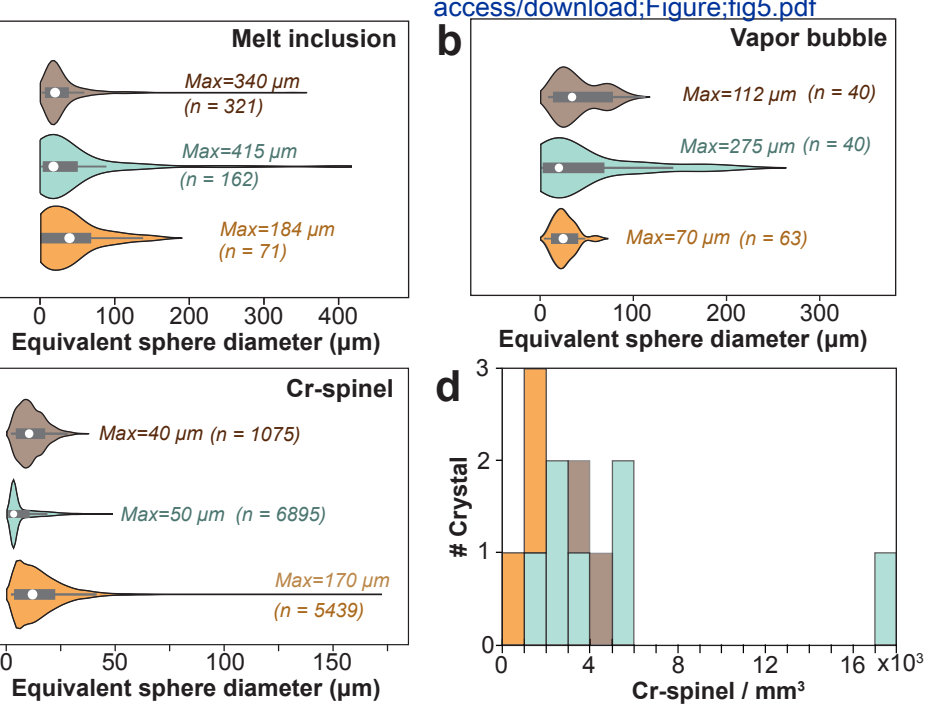
Skeletal elongated along [100]
Skeletal clusters
Polyhedral clusters
Click here to access/download;Figure;fig5.pdf
a
Melt inclusion
Max=340 µm
(n = 321)
Max=415 µm
(n = 162)
Max=184 µm
(n = 71)
0
100
200
300
400
Equivalent sphere diameter (µm)
b
Vapor bubble
Max=112 µm (n = 40)
Max=275 µm (n = 40)
Max=70 µm (n = 63)
0
100
200
300
Equivalent sphere diameter (µm)
c
Cr-spinel
Max=40 µm (n = 1075)
Max=50 µm (n = 6895)
Max=170 µm
(n = 5439)
0
50
100
150
Equivalent sphere diameter (µm)
d
Crystal
0
1
2
3
0
4
8
12
16
x10³
Cr-spinel / mm³

Figure

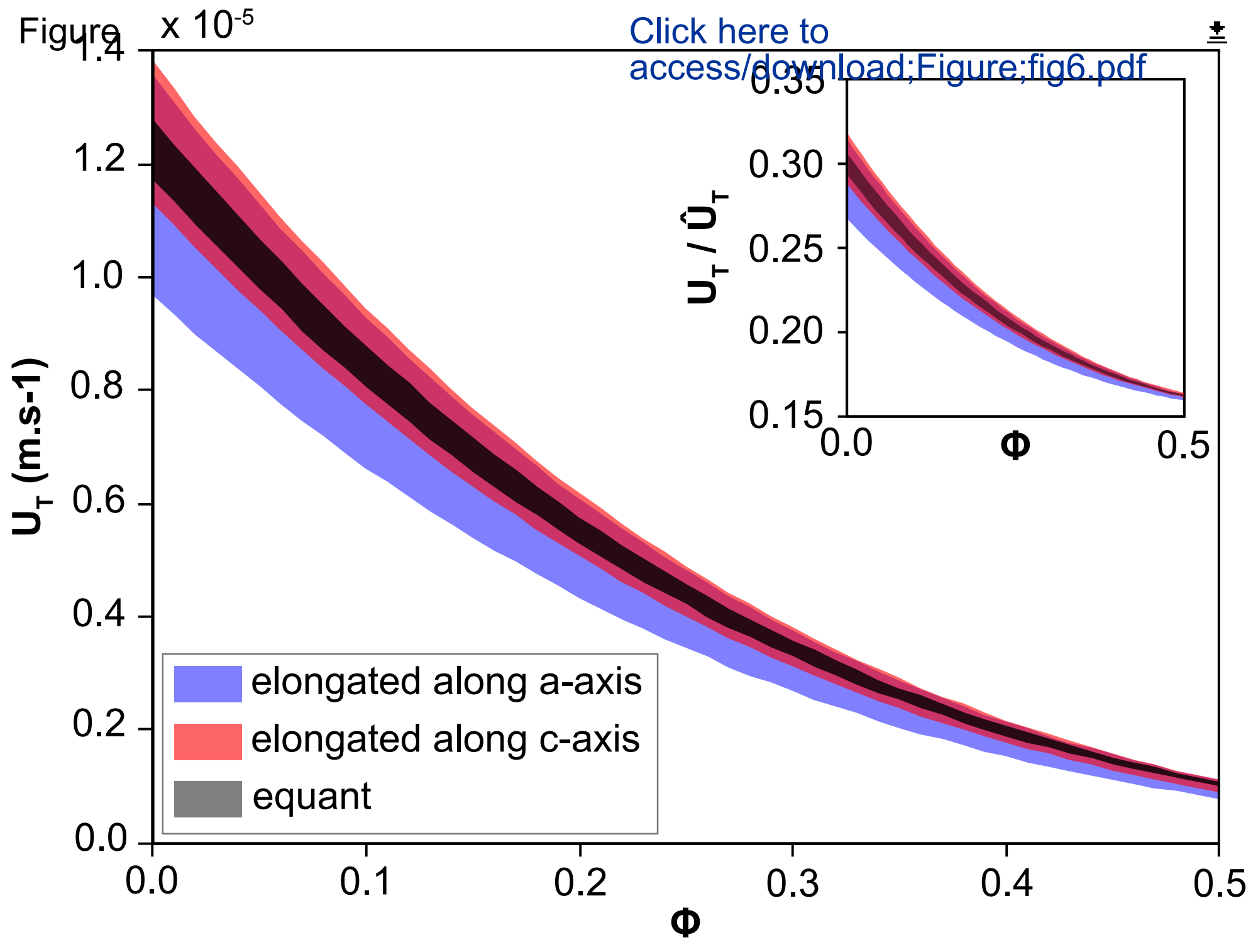
x 10-5
Click here to access/download;Figure;fig6.pdf
1.4
1.2
1.0
0.8
0.6
0.4
0.2
0.0
UT (m.s-1)
0.0
0.1
0.2
0.3
0.4
0.5
Φ
elongated along a-axis
elongated along c-axis
equant
0.35
0.30
0.25
0.20
0.15
UT / ÛT
0.0
0.5
Φ

Figure

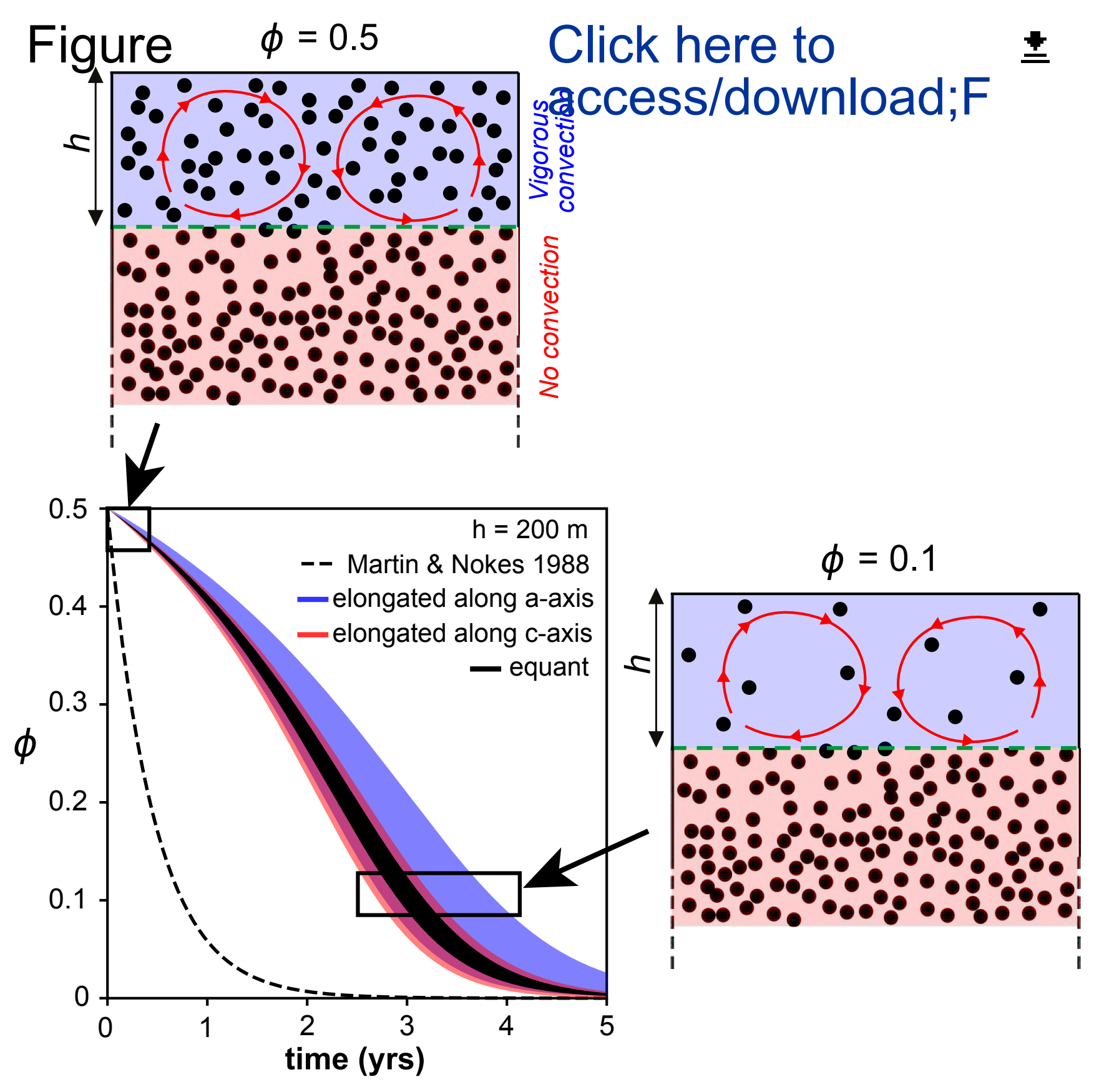

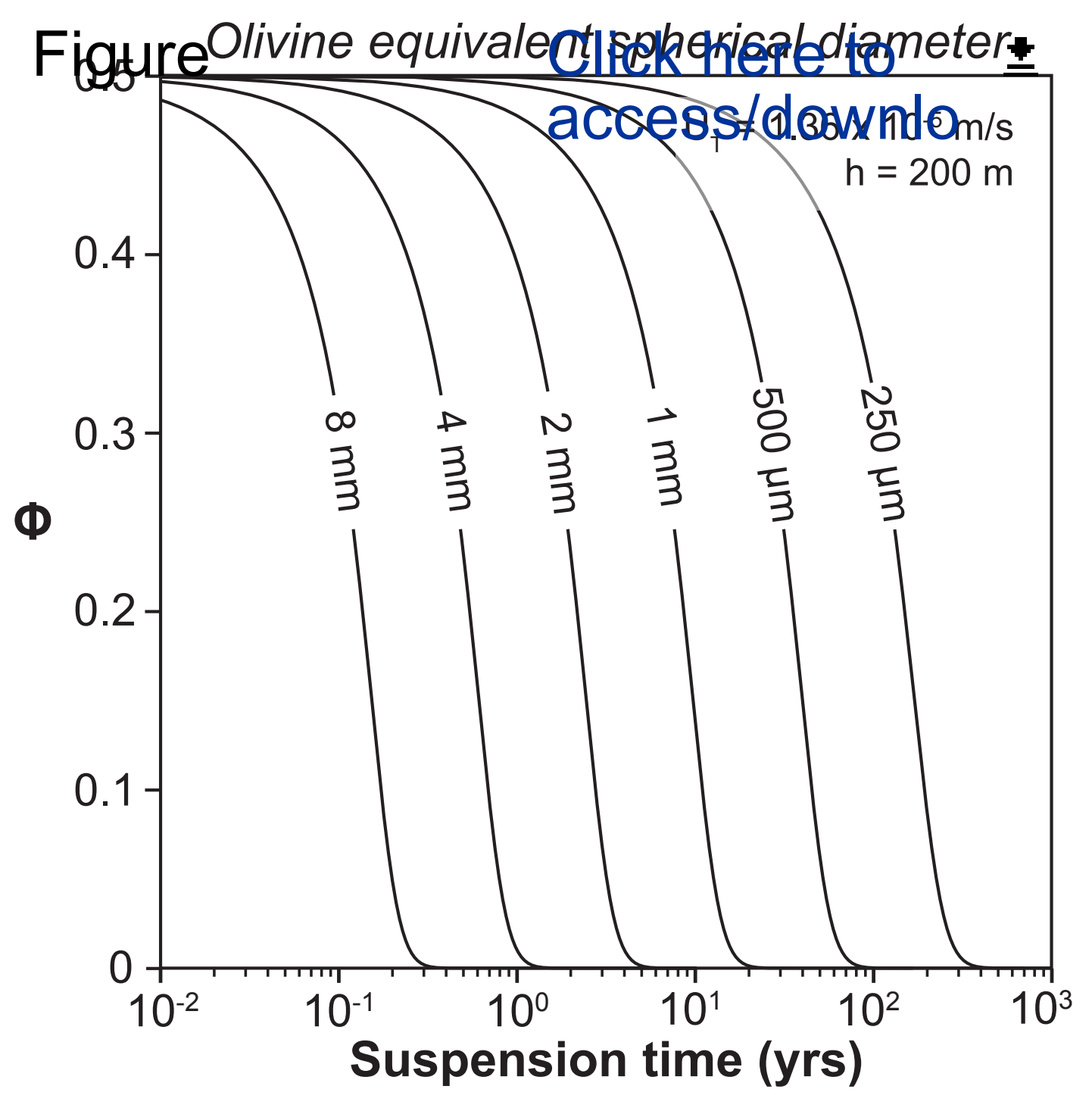
Olivine equivalent spherical diameter
Click here to access/downlo
w_t = 1.36 x 10^{-5} m/s
h = 200 m
8 mm
4 mm
2 mm
1 mm
500 µm
250 µm
Φ
0
0.1
0.2
0.3
0.4
0.5
10^{-2}
10^{-1}
10^{0}
10^{1}
10^{2}
10^{3}
Suspension time (yrs)

Table 1: Physical properties of the crystal and melt. Symbols used are ρ_l (melt density), η (melt viscosity), ρ_c (crystal density), U_{inj} (injection velocity).

Physical properties	**Value**	**Reference**
ρ_l	2750 kg m^{-3}	Mourey and Shea (2019)
η	30 Pa s	Giordano et al. (2008)
ρ_c	3400 ± 50 kg m^{-3}	Lynn et al. (2017); Mourey et al. (2022)
U_{inj}	10^{-3} m s^{-1}	_

Table 2: Olivine crystal dimensions along a = [100], b = [010], c = [001] axis, equivalent sphere diameter, density of olivine crystal, effect of inclusions (melt, Cr-spinel, vapor bubbles) on crystal density. Details on density calculations are in the supplementary material.

Olivine name	Morphology	[100] length (µm)	[010] length (µm)	[001] length (µm)	Density crystal with inclusions (kg m^{-3})	Olivine/crystal density difference due to inclusions (%)
k1820_ol1A	Skeletal cluster	2035	159	701	3253-3340	-3.20 to -2.90
k1820_ol4A	Skeletal cluster	1487	289	849	3212-3296	-4.45 to -4.11
k1820_ol2B	Skeletal crystal elongated along [100]	1916	353	729	3152-3239	-6.12 to -5.92
k1820_ol3A	Skeletal crystal elongated along [100]	1735	452	844	3312-3405	-1.32 to -1.15
k1820_ol14A	Skeletal crystal elongated along [100]	1517	832	330	3155-3230	-6.38 to -5.83
k1820_ol9A	Skeletal crystal elongated along [100]	872	351	479	3246-3328	-3.55 to -3.09
k1820_ol15A	Skeletal crystal elongated along [100]	705	297	347	3236-3326	-3.60 to -3.42
k1820_ol11A	Skeletal crystal elongated along [100]	1040	362	612	3143-3229	-6.41 to -6.17
k1820_ol10B	Skeletal crystal elongated along [100]	953	304	581	3339-3434	-0.47 to -0.33
k1820_ol8A_1	Polyhedral crystal elongated along [100]	923	391	600	3381-3480	+0.87 to +0.94
k1820_ol12A_1	Polyhedral crystal elongated along [100]	1565	580	1207	3381-3480	+0.11 to +0.16
k1820_ol12A_2	Polyhedral crystal elongated along [100]	1220	556	817	3355-3454	+0.11 to +0.16
k1820_ol12A_3	Polyhedral crystal elongated along [001]	1030	826	1238	3355-3454	+0.11 to +0.16
k1820_ol13A_1	Polyhedral crystal elongated along [100]	2311	961	1404	3353-3453	+0.08 to +0.09
k1820_ol13A_2	Polyhedral crystal elongated along [100]	631	464	619	3353-3453	+0.08 to +0.09
k1820_ol13A_3	Polyhedral crystal elongated along [100]	927	596	516	3353-3453	+0.08 to +0.09
k1820_ol13A_4	Polyhedral crystal elongated along [100]	1082	634	650	3353-3453	+0.08 to +0.09
k1820_ol5B_1	Polyhedral crystal elongated along [001]	1172	813	1261	3358-3457	+0.20 to +0.25
k1820_ol5B_2	Polyhedral crystal elongated along [100]	971	408	612	3358-3457	+0.20 to +0.25
k1820_ol5B_3	Polyhedral crystal elongated along [001]	532	350	684	3358-3457	+0.20 to +0.25
k1820_ol5B_4	Polyhedral crystal elongated along [001]	725	613	1209	3358-3457	+0.20 to +0.25
k1820_ol5B_5	Polyhedral crystal elongated along [001]	491	467	582	3358-3457	+0.20 to +0.25
k1820_ol5B_6	Polyhedral crystal elongated along [001]	307	250	371	3358-3457	+0.20 to +0.25
k1820_ol5B_7	Polyhedral crystal elongated along [001]	87	77	97	3358-3457	+0.20 to +0.25
k1820_ol5B_8	Polyhedral crystal elongated along [001]	81	233	250	3358-3457	+0.20 to +0.25

Table 3: List of the simulations and results. ξ is a coefficient that depends on the shape and orientation of the particle (see Eq. 17), %press. is the percentage of the contribution of pressure drag to the total drag force ($\int_S -p\,\boldsymbol{n}_s\,dS$ in Eq. 15), %frict. is the percentage of the contribution of viscous friction to the total drag force ($\int_S \tau\,dS$ in Eq. 15), U_T is the terminal settling velocity, ϕ is the solid volume fraction at the location of the crystal.

Run	Crystal	Orientation	Axis lengths a, b, c (μm)	ξ	% press.	% frict.	U_T at $\phi = 0$ (m s^{-1})
A1	Elongated along a-axis	*a-axis* aligned with the flow	3414; 983; 1648	83.6	21.3	78.7	1.36×10^{-5}
A2	Elongated along a-axis	*b-axis* aligned with the flow	3414; 983; 1648	102.8	31.9	68.1	1.10×10^{-5}
A3	Elongated along a-axis	*c-axis* aligned with the flow	3414; 983; 1648	117.2	50.3	49.7	9.67×10^{-6}
B1	Elongated along c-axis	*a-axis* aligned with the flow	1426; 1742; 3022	100.2	44.3	55.7	1.13×10^{-5}
B2	Elongated along c-axis	*b-axis* aligned with the flow	1426; 1742; 3022	99.7	38.0	62.0	1.14×10^{-5}
B3	Elongated along c-axis	*c-axis* aligned with the flow	1426; 1742; 3022	82.1	22.5	77.5	1.38×10^{-5}
C1	Equant	*a-axis* aligned with the flow	2040; 1942; 1978	88.4	35.6	64.4	1.28×10^{-5}
C2	Equant	*b-axis* aligned with the flow	2040; 1942; 1978	96.4	35.6	64.4	1.18×10^{-5}
C3	Equant	*c-axis* aligned with the flow	2040; 1942; 1978	90.8	38.3	61.7	1.25×10^{-5}